

Background-dependent effects of selection on subclonal heterogeneity

Ignacio Vázquez-García*^{†,1,2}, Francisco Salinas*,³ Jing Li,³ Andrej Fischer,¹ Benjamin Barré,³ Johan Hallin,³ Anders Bergström,¹ Elisa Alonso-Perez,⁴ Jonas Warringer,^{4,5} Ville Mustonen*^{†,1} and Gianni Liti*^{†3}

¹Wellcome Trust Sanger Institute, Hinxton, Cambridge CB10 1SA, United Kingdom

²Department of Applied Mathematics and Theoretical Physics, University of Cambridge, Cambridge CB3 0WA, United Kingdom

³Institute for Research on Cancer and Aging of Nice, CNRS UMR 7284, INSERM U1081, University of Nice Sophia Antipolis, 06107 Nice, France

⁴Department of Chemistry and Molecular Biology, University of Gothenburg, Gothenburg, Sweden

⁵Centre for Integrative Genetics (CIGENE), Department of Animal and Aquacultural Sciences, Norwegian University of Life Sciences, Ås, Norway

(Dated: July 27, 2016)

The contribution of pre-existing and *de novo* genetic variation towards clonal adaptation is poorly understood, but essential to design successful antibiotic or cancer therapies. To address this, we evolved genetically diverse populations of budding yeast, *S. cerevisiae*, consisting of $\sim 10^7$ diploid cells with unique haplotype combinations. We studied the asexual evolution of these populations under selective inhibition of DNA replication and cell metabolism by time-resolved whole-genome sequencing and phenotyping. All populations underwent clonal expansions driven by *de novo* mutations, but remained genetically and phenotypically diverse. Despite the genetic diversity of the founder cells, we observed recurrent adaptive mutations. However, the founding fitness variance limited the scope for adaptive mutations to expand. The clones exhibited continued evolution by widespread genome instability, rendering recessive *de novo* mutations homozygous and refining pre-existing variation. Our results show that three intertwined processes dominate the adaptive response: exploiting genetic backgrounds, *de novo* mutations and genome instability.

I. INTRODUCTION

The adaptive response of a cell population can thwart therapeutic control of a wide spectrum of diseases, from bacterial and viral infections to cancer. A prototypical scenario arises when individuals in a population acquire heritable genetic or non-genetic changes to adapt and thrive in a new environment (Toprak et al., 2012; Marusyk et al., 2014; Balaban et al., 2004). Since the seminal findings by Luria and Delbrück that phage-resistant bacteria can acquire adaptive mutations prior to selection (Luria and Delbrück, 1943), measuring the fitness effects and dynamics of mutations has been key to map the principles of evolutionary adaptation (Barrick and Lenski, 2013). The focus has typically been on characterizing few mutations at a time under the implicit assumption that beneficial mutations are rare, treating pre-existing and acquired mutations separately. However, many mutations are often simultaneously present in a population, which result in fitness differences between individuals that selection can act upon (Parts et al., 2011; Lang et al., 2013; Levy et al., 2015). Recent findings indicate that genetic heterogeneity can thus play a major role in the development of resistant bacterial infections (Young et al., 2012; Lieberman et al., 2014) and in cancer recurrence (Gerlinger et al., 2012; Landau et al., 2013; Eirew et al., 2014). Given that mutations in asexual populations are physically linked in the genome, their fates are mutually dependent and selection can only act on these sets of variants in their entirety (Lang et al., 2011). As a result, genetic diversity can change the evolutionary fate of new adaptive mutations by limiting the number of backgrounds where they can still outcompete the fittest extant individuals. To what extent then can the adaptive response be attributed to genetic variation already present and how much to acquired? How do the aggregate effects of mutations influence adaptive trajectories?

To address these questions, we investigated the interaction between pre-existing (or background) genetic variation and new mutations in a population of diploid cells with unique combinations of alleles. The cells originate from two diverged *S. cerevisiae* strains (Fig. 1A). We carried out 12 rounds of random mating and sporulation (meiosis) between DBVPG6044, a West African palm wine strain (WA), and YPS128, a North American oak tree bark strain (NA) (Parts et al., 2011). The cross population (WxNA) consisted of 10^7 - 10^8 unique haplotypes, with a pre-existing variant segregating every 230 bp on average. We further identified 82 SNPs acquired *de novo* during the crossing phase from genome sequences of 173 founder individuals, which is consistent with a mutation rate of approximately 3×10^{-10} SNPs per site per cell division, close to empirical estimates in other yeast strains (Zhu et al., 2014). Starting from WA, NA and WxNA founders, we asexually evolved populations in serial batch culture with inhibitors of DNA replication (hydroxyurea) and of cellular

* Equal contribution from these authors.

† For correspondence: ivg@sanger.ac.uk, vm5@sanger.ac.uk, gianni.liti@unice.fr

growth and metabolism (rapamycin) at concentrations impeding, but not ending, cell proliferation. These drugs were chosen as generic instances of strong selective pressures that act on fundamental growth-related pathways with known targets. We derived replicate lines of WA, NA (2 each in hydroxyurea and rapamycin) and WAxNA (6 in hydroxyurea, 8 in rapamycin and 4 in a control environment). We monitored evolutionary changes by whole-genome sequencing of populations after 2, 4, 8, 16 and 32 days, as well as clonal isolates at 0 and 32 days (Table S1). Finally, we measured growth phenotypes at the initial and final time point for a subset of populations, and quantified the relative fitness contributions of background and *de novo* variation using a genetic cross.

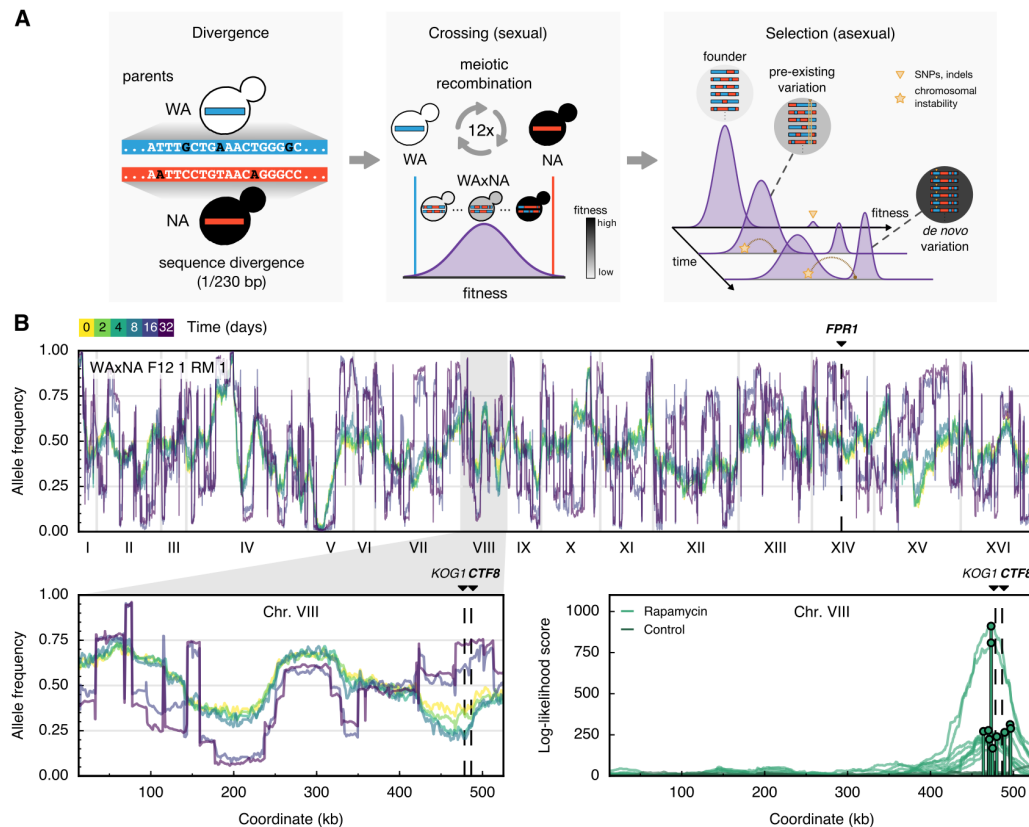


Figure 1: Study overview and genome-wide allele frequency changes. (A) Two diverged parental lines of *S. cerevisiae* were crossed for twelve rounds, generating a large ancestral population of unique haplotypes. These diploid cells were asexually evolved for 32 days in stress and control environments and their adaptation was studied by whole-population and isolate sequencing and phenotyping. Populations evolved resistant macroscopic subclones driven by beneficial *de novo* mutations and by individuals whose parental allele configurations, i.e. genetic backgrounds, provided a resistance phenotype. (B) Genome-wide allele frequency q_i^{WA} of pre-existing parental variants as observed for a representative population in rapamycin (WAxNA F12 1 RM 1). Bottom left panel: Zoomed inset of the shaded region shows allele frequency changes in chromosome VIII during selection in rapamycin. Early time points 2, 4 and 8 show localized allele frequency changes at 460-490 kb due to a beneficial allele sweeping with hitchhiking passengers. Late time points 16 and 32 show abrupt jumps between successive loci that reflect the parental haplotype of the emerging subclone(s). In case of a fully clonal population, the allele frequencies would be at 0, 0.5 and 1.0 corresponding to the background genotypes NA/NA, WA/NA, and WA/WA of a diploid clone that reached fixation. Bottom right panel: We tested a model where each allele is proposed to be a driver under selection, changing in frequency and causing nearby linked passenger alleles to do so. Top log-likelihood scores are shown for all populations in this region of interest ([‘Materials and methods’](#)). We validated the $CTF8^{NA}$ allele to be strongly beneficial for rapamycin resistance (Fig. S10).

II. RESULTS

Two regimes of selection became readily apparent in both sequence and phenotype. Initially, there were local changes in the frequency of parental alleles under selection (Fig. 1B). Over time, macroscopic subclonal populations arose and expanded, depleting the pool of genetic diversity. These successful genotypes persisted in time, manifested by broad jumps in the allele frequency visible across the genome (Fig. 1B and Fig. S2). But what drives these expansions: is it the founder haplotypes themselves, *de novo* mutations relegating the parental variation to the role of passengers, or their combined action?

Selective effects on background variation

To determine the adaptive value of background variation, we identified regions where local allele frequencies changed over the time course of the selection experiments. Frequency differences over time indicate that selection is acting on background alleles, and linked passenger mutations also change in frequency by genetic hitchhiking (Illingworth et al., 2012). We performed a systematic scan for background variants under selection using data up to 4 days, when no population yet had detectable subclones which would distort this signal ('Materials and methods'). A region of interest was found in chromosome VIII (coordinates ~460-490 kb) in all WAXNA populations under rapamycin (Fig. 1C). We evaluated two candidate genes in this region by reciprocal hemizyosity, validating the *CTF8*^{NA} allele to increase rapamycin resistance (Fig. S10). *CTF8* harbors two background missense variants and has previously been implicated in sensitivity to rapamycin, although the mechanism remains unknown (Parsons et al., 2004). Carrying the *CTF8*^{NA} allele confers a 36% growth rate advantage. *KOG1*, which falls within the same region and is a subunit of the TOR complex 1 (TORC1), differs by seven missense mutations between the parents. However, reciprocal hemizygous deletions only revealed a modest fitness difference between WA and NA sequences of *KOG1*. We did not find events that replicated across all populations in hydroxyurea.

Pervasive selection of macroscopic subclones

To reconstruct clonal expansions in the WAXNA populations we used background genetic variants as markers. Using the cloneHD algorithm (Fischer et al., 2014), we inferred the subclonal genotypes and their frequency in the populations, both of which are unknown *a priori* ('Materials and methods'). We found at least one subclone in all populations under selection, but none in the control environment (Fig. 2 and Fig. S4). No population became fully clonal during the experiment, with subclone frequencies stabilizing after 16 days in several rapamycin populations. Similarly, WA and NA populations under selection underwent adaptation as evidenced by *de novo* mutation frequencies (Fig. S3).

To genetically characterize subclones, we isolated and sequenced 44 clones drawn from WAXNA populations after the selection phase ('Materials and methods'; Fig. S6). From population and isolate sequence data, we observed 19 recurrent *de novo* mutations in the hydroxyurea targets *RNR2* and *RNR4* during hydroxyurea selection and in the rapamycin targets *FPR1* and *TOR1* during rapamycin selection (Table S2). Each of these driver mutations had a drug resistant growth rate phenotype (Figs. S9 and S10) and carried a private background combination of ~31,000 passenger SNPs on average, compared to other sequenced isolates. *FPR1* mutations were always homozygous and likely to inactivate the gene or inhibit its expression. In contrast, *TOR1* mutations were heterozygous while we found *RNR2* and *RNR4* mutations in both heterozygous and homozygous constellations. All driver mutations occurred in highly conserved functional domains. The variant allele fractions of these mutations mirrored the inferred subclonal dynamics (Fig. 2A and C, and Figs. S3 and S4).

Clonal expansions were also evident by changes in the fitness distribution of cells. We established this by phenotyping 96 randomly isolated individuals from 3 populations per environment at 0 and 32 days, as well as the 44 sequenced individuals at 32 days (Fig. 2B and D). In rapamycin selection, the phenotype distribution became bimodal after 32 days, reflecting the fitness of subclones substantially improving with respect to the mean fitness of the bulk population. The clonal subpopulation divided on average twice as fast as the ancestral population. Sequenced isolates with driver mutations in *FPR1* and *TOR1* were on the leading edge of the phenotype distribution, far ahead of the bulk. Furthermore, the bulk component showed a 10% average improvement, possibly due to selection of beneficial genetic backgrounds. Conversely, bimodality was only detected in one population in hydroxyurea selection (WAXNA F12 1 HU 3), where the clonal peak grew 22% faster and the bulk 16% faster on average compared to the ancestral. Isolates with *RNR2* driver mutations fell onto the leading edge of the fitness distribution. These six isolates originated from the same expanding subclone and two of them had 13% faster growth rate than the remaining four, although they all shared the same heterozygous *RNR2* driver mutation. In both of these clones, we found a large region in chromosome II

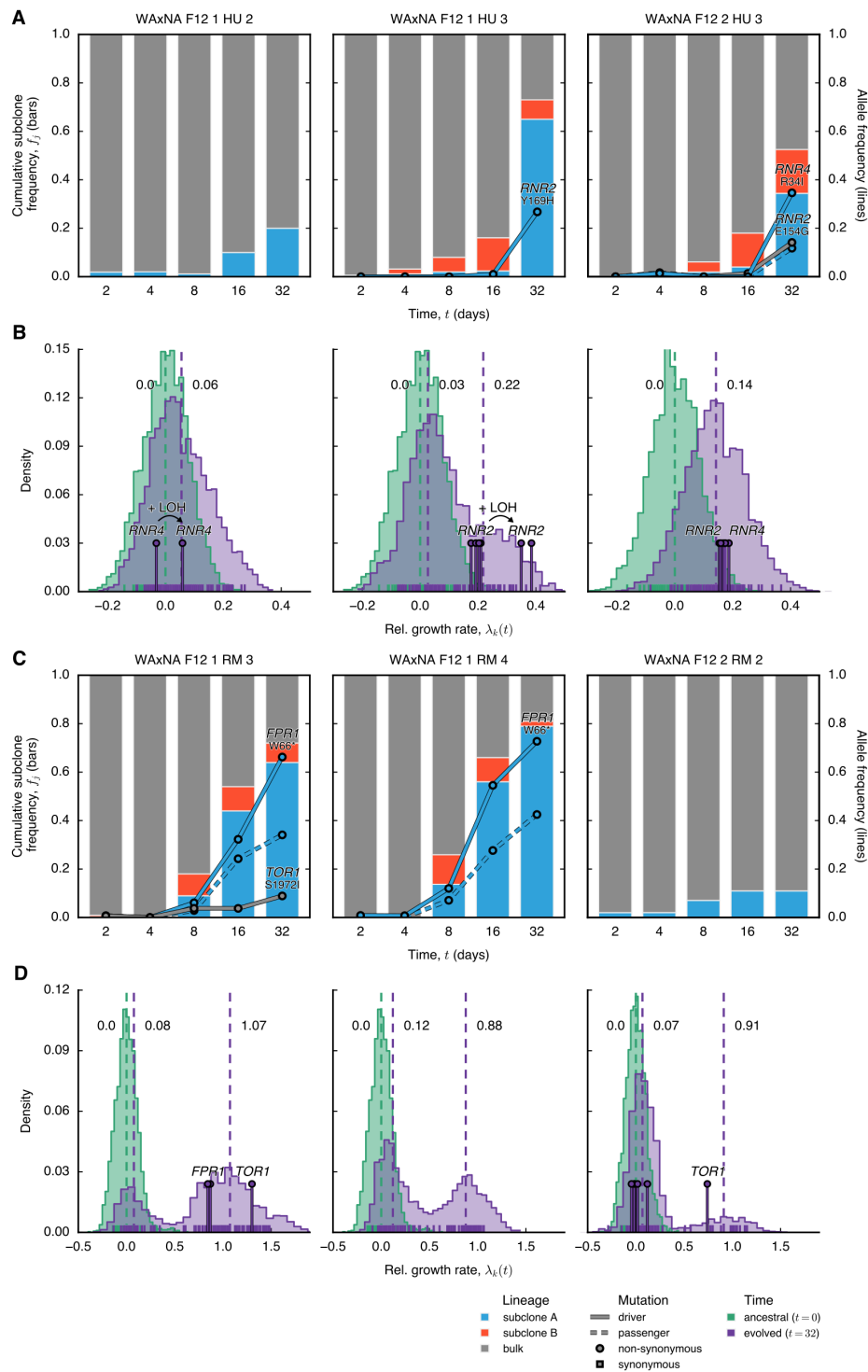


Figure 2: Reconstruction of subclonal dynamics. Competing subclones evolved in (A, B) hydroxyurea and (C, D) rapamycin experienced a variety of fates. (A and C) Time is on the x -axis, starting after crossing when the population has no macroscopic subclones. Cumulative haplotype frequency of subclones (bars) and allele frequency of *de novo* mutants (lines) are on the y -axis. Most commonly, selective sweeps were observed where a spontaneous mutation arose and increased in frequency. Driver mutations are solid lines and passenger mutations are dashed lines, colored by subclone assignment; circles and squares denote non-synonymous and synonymous mutations, respectively. (B and D) Variability in intra-population growth rate λ , estimated by random sampling of 96 individuals at initial ($t=0$ days, green) and final ($t=32$ days, purple) time points ($n=32$ technical replicates per individual). Mean growth rates by individual are shown at the foot of the histogram (Fig. S7). The posterior means of the distribution modes fitted by a Gaussian mixture model are indicated as dashed lines. The fitter individuals (pins) carry driver mutations, measured by targeted sampling and sequencing.

to have undergone loss of heterozygosity (LOH), offering a putative genetic cause for their growth advantage (Fig. 3C).

Diversification and genome instability

Surprisingly, we found several of the driver mutations to exist in homozygous rather than heterozygous states (Table S2). We hypothesized that genome instability, causing widespread LOH, can significantly contribute to adaptation in diploid populations. To detect mechanisms of genome instability, we used heterozygous genetic variants as markers. Firstly, we used the sequences of haploid individuals from the ancestral population, drawn before the last round of crossing, to create *in silico* diploid genomes and calculate the length distribution of homozygous segments. Similarly, we measured the length distribution of homozygous segments from evolved isolate genomes. We observed a significant increase of long homozygosity tracts in the evolved clones – a hallmark of LOH (Fig. 3A). Secondly, we directly counted LOH events in populations using multiple sequenced isolates from the same expanding subclone (‘Materials and methods’). We identified a minimum of 6 events per genome per clone (Fig. S6). Whilst this estimate is a lower bound and is limited due to the number of sequenced individuals per subclone, the LOH rates are substantial. An alternative route to homozygosity was observed in a single clone found to be haploid (clone C1 in WAXNA F12 1 RM 1) and therefore homozygous genome-wide. This haploid clone is closely related to a diploid clone (C3) from the same population and both

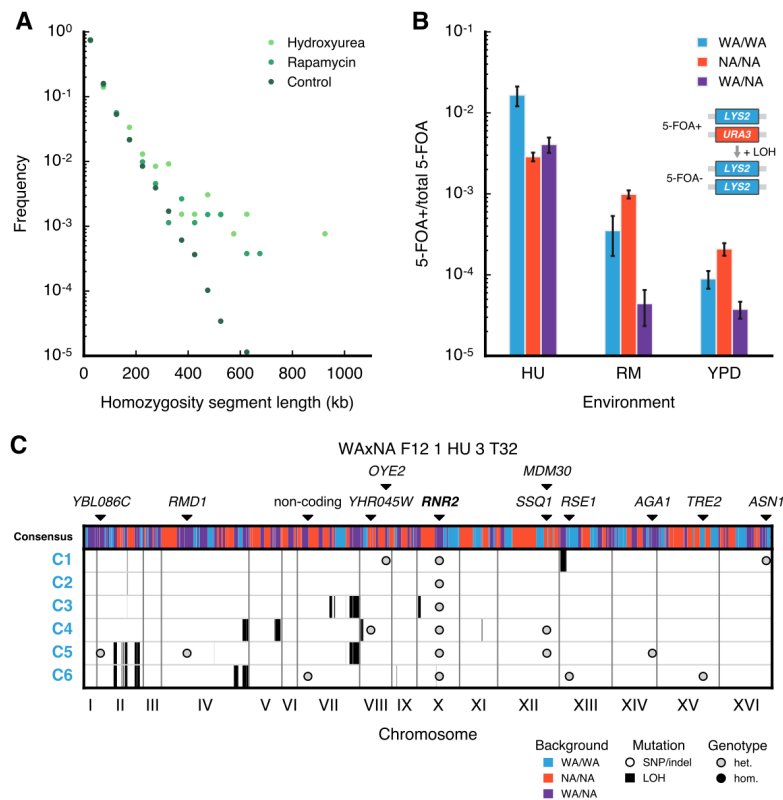


Figure 3: Pervasive genome instability. (A) The length distribution of homozygous segments, in bins corresponding to 50-kb increments, shows an excess of long homozygosity tracts above 300 kb in hydroxyurea and rapamycin (KS-test, $P < 0.01$). Ancestral haploid isolates are used to compare a set of *in silico* diploid genomes to evolved diploid isolates. Only unrelated isolate backgrounds were included. (B) Background- and environment-dependent rates of loss-of-heterozygosity were measured in a fluctuation assay by loss of the URA3 marker. 5-FOA+ colonies indicate loss of the marker. LOH rates were elevated in hydroxyurea compared to the control environment and manifested background-dependent effects between the parents and their hybrid. The mean frequency of 5-FOA+ colony-forming units (c.f.u.) is shown. Error bars indicate the standard error of the mean. (C) Consensus genotype of six related isolates from the WAXNA F12 1 HU 3 population, each carrying a shared *RNR2* heterozygous mutation (circles) and private regions with LOH (segments). Chromosome II has undergone extensive LOH in isolates C5 and C6, which have 13% faster growth rate compared to C1-C4 (Fig. 2D, center panel).

clones share the same *FPR1* W66* *de novo* mutation (Fig. S6B). These data are consistent with the appearance of the *FPR1* heterozygous mutation in an ancestral diploid clone that took two independent routes – focal LOH or meiosis – to unveil the recessive driver mutation. Altogether, we find that genome instability can render *de novo* mutations homozygous as a necessary event in a multi-hit process towards drug resistance.

The stress environments themselves have an active role in accelerating genome evolution by chromosomal instability. Using a fluctuation assay, we investigated the effect of the genetic background and of the selective environment on chromosomal instability by tracking the loss of the *URA3* marker. Consistent with previous studies (Barbera and Petes, 2006), replication stress induced by hydroxyurea caused an increase in LOH rates. We also observed a background-dependent increase in LOH in rapamycin (Fig. 3B).

Fitness effects of background and *de novo* variation

Finally, we sought to partition and quantify the individual fitness contributions of pre-existing and *de novo* genetic variation. To this end, we designed a genetic cross where background and *de novo* variants were re-shuffled to create new combinations (Fig. 4A). We randomly isolated diploids from both ancestral and evolved populations, sporulated these and determined whether the derived haploids contained wild-type or mutated *RNR2*, *RNR4*, *FPR1* and *TOR1* alleles. We then crossed haploids to create a large array of diploid hybrids where all genotypes (+/+, +/-, -/-) for each of these genes existed in an ensemble of backgrounds, thus recreating a large fraction of the genotype space conditioned on the presence or absence of driver mutations. We measured the growth rates of both haploid spores and diploid hybrids, estimating and partitioning the variation in growth rates contributed by the background genotype and *de novo* genotypes using a linear mixed model ('Materials and methods'). After conditioning for *RNR2*, *RNR4*, *FPR1* and *TOR1* driver mutation status, a large fraction of the phenotypic variance still remained, reflecting the effect of the genetic backgrounds in which they emerged (Fig. 4C and D). In fact, under hydroxyurea exposure, background genetic variation accounted for an estimated 51% of the growth rate variance, more than twice the estimated 23% contributed by *RNR2* and *RNR4* *de novo* mutations. This result directly implies that moderate effect *de novo* mutations must arise on favorable genetic backgrounds to give rise to macroscopic subclones. In contrast, under rapamycin exposure, the pre-existing genetic variation accounted for only 22% of the variance, much less than the 70% attributed to *FPR1* and *TOR1* mutations. Such large-effect mutations can expand in a vast majority of backgrounds, explaining how they can almost entirely determine the motion of the fitness distribution (Fig. 2D). The ensemble average over backgrounds showed that the mean effect of *RNR2*, *RNR4* and *TOR1* mutations was fully dominant and highly penetrant regardless of the background (Fig. 4E and F). In contrast, *FPR1* mutants were recessive and only increased growth rate when homozygous, again irrespective of the background (Fig. 4F). Taken together, these data are consistent with the aggregation of small-effect, pre-existing variants that add up and substantially contribute to fitness in both selection environments.

III. DISCUSSION

Populations adapt to external challenges by exploiting pre-existing variation and discovering *de novo* solutions, but how these variants jointly influence evolution is not well understood. The rate of adaptation depends on multiple factors such as population size, mutation rate and ploidy (Barrick and Lenski, 2013; Selmecki et al., 2015; zur Wiesch et al., 2011). Our results show that sufficiently large populations could readily find beneficial *de novo* mutations, but their adaptive trajectories were simultaneously shaped by pre-existing and *de novo* variation with overlapping timescales. Our findings are relevant to understand large asexual populations with extensive pre-existing variation, such as pathogens and cancer, which easily reach sizes of billions of cells. Despite the large initial genetic heterogeneity, the same driver mutations recurred in multiple populations, indicating convergent evolution towards a restricted number of molecular targets. This is a key aspect to be able predict the outcome of selection, and thus to what extent it could inform the design of second line therapies in the treatment of bacterial and viral infections or cancer. Noticeably, the substantial genotypic and phenotypic diversity that remained after selection could well be a potent substrate for populations to escape from the application of second line therapies. Clearly, whether or not these results hold more generally needs to be studied across systems.

Our results show that, not only was there a constant supply of new beneficial mutations, but selection concomitantly acted on pre-existing variation through its combined effects on fitness. New mutations entered the population and the bulk of the population steadily improved. In some cases, acquired mutations were sufficient to determine the motion of the fitness distribution, such as *TOR1* mutations in rapamycin. Conversely, the pre-existing fitness variance influenced the fate of *de novo* drivers like *RNR2* and *RNR4* mutations, which needed to land on a favorable background to be competitive. Therefore, detecting a known driver mutation without a measurement of the background fitness distribution would be insufficient to predict its fate. Controlling and

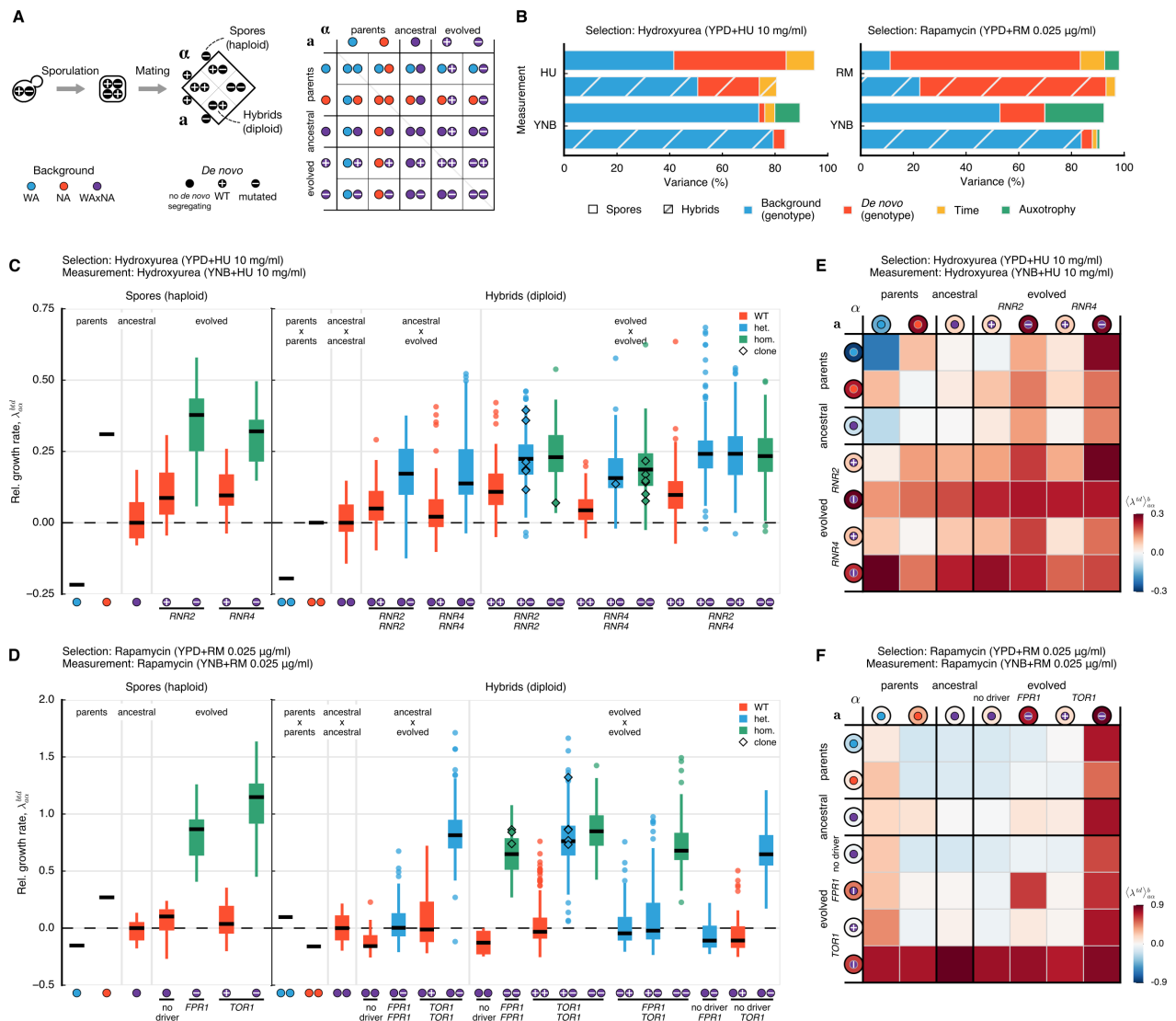


Figure 4: Fitness contribution of genetic background and *de novo* mutations. (A) To determine fitness effects of background variation and *de novo* mutations in hydroxyurea (*RNR2*, *RNR4*) and rapamycin (*FPR1*, *TOR1*), we isolated individuals from ancestral and evolved populations. From these diploid cells, we sporulated and selected haploid segregants of each mating type. Spores with mutations in *RNR2*, *RNR4* and *TOR1* were genotyped to test if they carry the wild-type or mutated allele. We crossed the *MATa* and *MATα* versions to create hybrids (48×48 in hydroxyurea and 56×56 in rapamycin). Independent segregants were used to measure biological variability of ancestral and evolved backgrounds. All panels follow this legend. (B) Variance decomposition of the growth rate of spores (solid) and hybrids (hatched) that can be attributed to different components using a linear mixed model. Estimates of variance components are obtained by restricted maximum likelihood (Fig. S13 and Table S7). (C and D) Relative growth rate, λ , measured with respect to the ancestral population for multiple combinations (background genotype, b ; *de novo* genotype, d ; time of sampling during the selection phase, t ; auxotrophy, x) and averaged over measurement replicates. Medians and 25%/75% percentiles across groups are shown, with medians as horizontal black lines and colored by *de novo* genotype [wild-type $+/+$ (red); heterozygote $+/-$ (blue); homozygote $-/-$ (green)]. Outliers (circles) and isolated, selected clones with matching genotypes (diamonds) are highlighted. (E and F) Ensemble average of the growth rate of spores, $\langle \lambda^{td} \rangle_{\{a, \alpha\}}$, and hybrids, $\langle \lambda^{td} \rangle_{a\alpha}$. An extended version of the figure with all combinations and controls can be found in Figs. S11 and S12, respectively.

balancing the fitness effects of background and *de novo* mutations in response to these stress environments may be possible, as their effects can be modulated by inhibiting global regulators (Jarosz and Lindquist, 2010).

We observed a balance between the loss of diversity due to selection, and active diversification mechanisms that partially re-established and refined existing variants. The background not only contributed substantially to fitness, but was also continuously re-configured by genome instability, diversifying the clones as they expanded – the moving target metaphor of resistance evolution captured in action. Although these rearrangements were mostly copy number neutral, they lead to phenotypic change by changing scores of mutations from heterozygous to homozygous state in a single step. Such chromosomal rearrangements represent a key mechanism in shaping genome diversity in asexual organisms (Flot et al., 2014; Weir et al., 2016; Ford et al., 2015) and in somatic evolution of cancer (Stephens et al., 2011), where cells accumulate a genetic load during tumor development that LOH can phenotypically reveal. Recently developed genome editing approaches may enable localizing and measuring the fitness effect of specific LOH regions (Sadhu et al., 2016). Equally, chromosomal rearrangements also had a major effect on *de novo* variants, as recessive *FPR1* mutations needed a second hit by LOH for resistance. Taken together, we hope our results will stir work towards better theoretical and empirical understanding of the complex interplay of selection simultaneously acting on pre-existing and *de novo* genetic variation, and of the role of genome instability continuously molding the genomes in a population.

IV. MATERIALS AND METHODS

The experimental methods and quantitative analyses of this study are presented in Section IV.A ‘Experimental methods’. In Section IV.B ‘Theory and data analysis’, we present the definition of the model for localization of drivers amongst hitchhiking passengers and the probabilistic inference method for subclonal reconstruction. Furthermore, we discuss the model for the estimation of variance components from background-averaged fitness measurements. Supplementary figures and tables are appended at the end of the ‘Materials and methods’. Code and data are available from the GitHub repository (<https://github.com/ivazquez/gv-paper-2016>).

A. Experimental methods

Evolution assays

In our study, we begin with two yeast strains which have diverged over millions of years (*diversification* phase), that are randomly mated by meiotic recombination to generate a large pool of recombinant mosaic haplotypes (*crossing* phase), followed by selecting a fraction of the population under stress without severe bottlenecks (*selection* phase).

Diversification phase

Parental strains were derived from a West African strain (DBVPG6044; *MAT α* , *ura3::KanMX*, *lys2::URA3*, *ho::HphMX*) isolated from palm wine and a North American strain (YPS128; *MAT α* , *ura3::KanMX*, *ho::HphMX*) isolated from oak tree (Table S3). Hereafter we refer to these strains as WA and NA, respectively. These strains were selected from two diverged *S. cerevisiae* lineages and feature 52,466 single-nucleotide differences uniformly distributed across the genome (see ‘Sequence analysis’).

Crossing phase

The selection experiments were carried out using WA, NA, WAXNA F₂ and WAXNA F₁₂ founder populations derived from hybrids between WA and NA. The WAXNA F₂ and F₁₂ populations were respectively generated from the F₁ and F₁₁ hybrids between WA (*MAT α* , *ura3::KanMX*, *lys2::URA3*, *ho::HphMX*) and NA (*MAT α* , *ura3::KanMX*, *ho::HphMX*).

The WAXNA F₁/F₁₁ diploid populations were expanded in YPDA and sporulated in solid KAc medium (2% potassium acetate, 2% agar) for 14 days at 23 °C. Sporulation of diploids was confirmed by visual inspection of asci. Over 90% of sporulation efficiency was observed after 14 days. Any remaining unsporulated cells were selectively removed using the ether protocol (Parts et al., 2011; Dawes and Hardie, 1974). The haploid population was subjected to mass mating according to the protocol described by Parts et al. (2011). Briefly, the asci were resuspended in 900 μ l of sterile water and digested with 100 μ l of zymolase (10 mg ml⁻¹) for 1 hour at 37 °C. The cells were washed twice with 800 μ l of sterile water, vortexed for 5 minutes to allow spore dispersion, plated in YPDA and incubated for 2 days at 23 °C. The YPDA plates were replica plated in

minimal medium to select diploid cells (*MATa/MAT α* , *LYS2/lys2::URA3*). The WAXNA F₂/F₁₂ generation was collected from the plates and used as a founder population for the selection experiments as well as stored at -80°C as a frozen stock.

Selection phase

In the selection phase, WA, NA, WAXNA F₂ and WAXNA F₁₂ founder populations (referred to as *ancestral*) were evolved asexually in two selective environments and one control environment. Where indicated, the selective media were supplemented with hydroxyurea (HU) at 10 mg ml^{-1} or rapamycin (RM) at $0.025\text{ }\mu\text{g }\mu\text{l}^{-1}$. We serially propagated multiple replicate populations over a period of 32 days (~ 200 generations), which we refer to as *evolved* populations. Every two days, 10% of the total cell population was transferred to fresh plates at constant drug concentration until day 34. WA and NA populations are labeled by their background, the environment in the selection phase and the selection replicate, e.g. NA RM 1. WAXNA populations are labeled by background, number of crosses, cross replicate, selection environment and selection replicate, e.g. WAXNA F12 2 HU 1. Time series samples are labeled from T0 to T32 and isolate clones carry a suffix, e.g. C1, C2, etc.

We followed the evolution of these populations over the course of the experiment using whole-genome sequencing and phenotyping of the bulk population, of ancestral and of evolved isolates. Whole-population sequencing was performed after $t = 0, 2, 4, 8, 16$ and 32 days, and ancestral and evolved individuals were also sequenced (Table S1). Genomic DNA was extracted from the samples using the ‘Yeast MasterPure’ kit (Epicentre, USA). The samples were sequenced with Illumina TruSeq SBS v4 chemistry, using paired-end sequencing on Illumina HiSeq 2000/2500 at the Wellcome Trust Sanger Institute. Sequence data for the parental strains and the ancestral individuals were previously submitted to the SRA/ENA databases under study accession no. ERP000780 and the NCBI BioProject under accession no. PRJEB2608. Sequence data for the time-resolved populations and the evolved individuals have been submitted to the SRA/ENA databases under study accession no. ERP003953 and the NCBI BioProject under accession no. PRJEB4645.

Random and targeted clone isolation

We isolated ancestral and evolved individuals from representative selection experiments to characterize their individual genome sequences and their fitness. Each sample underwent serial dilution to attain a single-cell bottleneck, plated on YPDA. We isolated individuals from both ancestral populations (WAXNA F12 1, WAXNA F12 2) and 6 evolved populations (WAXNA F12 1 HU 2, WAXNA F12 1 HU 3, WAXNA F12 2 HU 3, WAXNA F12 1 RM 3, WAXNA F12 1 RM 4, WAXNA F12 2 RM 2) to measure the initial and final fitness distribution. 96 colonies were randomly picked from each population to span a range of fitness. We measured their growth rate using the high-resolution scanning platform described in ‘Growth phenotyping’.

Furthermore, we isolated individuals at the fitter end of the phenotype distribution, possibly harboring driver mutations. Since adaptation to one environment typically results in fitness gains or losses in other environments, we profiled 96 individuals from each selection experiment with an array of 6 different environments (YPD, HU at 10 mg ml^{-1} , RM at $0.025\text{ }\mu\text{g }\mu\text{l}^{-1}$, galactose at 2%, heat at 40°C and sodium arsenite at 1.5 mM) to discriminate cells based on their phenotypic response. After visual inspection of shared effects across environments, we tested genetic markers by PCR/digestion and targeted resequencing of *de novo* mutations identified from the genome analysis of whole populations. In the hydroxyurea experiment, a heterozygous mutation in *RNR4* was genotyped by PCR followed by *BanI* digestion. In the rapamycin experiment, heterozygous *DEP1* and *INP54* *de novo* mutations were genotyped using PCR, followed by *AluI* digestion and confirmed by Sanger sequencing in a subset of samples. We chose a total of 44 clones (22 per environment) for whole-genome sequencing (Table S1).

Engineered genetic constructs

We selected two genes in which we found putative loss-of-function mutations in hydroxyurea (*RNR2*, *RNR4*) and five genes in rapamycin (*CTF8*, *DEP1*, *FPR1*, *TOR1*, *YNR066C*) and engineered gene deletions to confirm whether their knockouts are beneficial. We also built hemizygous strains to determine the adaptive value of background variation in putative driver genes, by engineering in or out ancestral or evolved alleles in opposite backgrounds. For pre-existing variants, the test for reciprocal hemizygosity uses one-step PCR deletion with *URA3* as a selectable marker. Starting from haploid versions of the WA and NA strains (either *MATa*, *ho::HygMX*, *ura3::KanMX* or *MAT α* , *ho::NatMX*, *ura3::KanMX*), we deleted the candidate genes and constructed all possible combinations of reciprocal hemizygous strains (Fig. S8). The deletion in the haploid strain

was confirmed by PCR and then crossed with the opposite mating type to generate the hemizygous hybrid strains (Steinmetz et al., 2002; Cubillos et al., 2011; Salinas et al., 2012). To test driver *de novo* mutations, we engineered reciprocal hemizygous deletions for two clones carrying heterozygous mutations in *RNR2* and *TOR1*. The gene deletion was performed using the dominant selectable marker *NatMX* and we used Sanger sequencing to identify the deleted allele (wild-type or mutated copy).

Genetic cross

We sought to measure the fitness contributions of pre-existing and *de novo* mutations using a genetic cross. To do so, we designed a large-scale cross where both ancestral and evolved genetic backgrounds were re-shuffled in new combinations and tested for fitness with and without drugs. The genetic cross included the *parents*, *ancestral* and *evolved* isolates. The WA and NA haploid parents were used in *MATa*, *ura3* and *MAT α* , *lys2* configurations. We derived haploid lines by sporulation on KAc medium from the ancestral and evolved clones. Only tetrads with four viable spores were chosen for continuation in the experiment. Spores were genotyped for mating type (*MATa*, *MAT α*) using tester strains and for auxotrophies (*ura3*, *lys2*) by plating on dropout medium. We chose spores from tetrad configurations with the mating marker co-segregating as *MATa*, *ura3* or *MAT α* , *lys2*, allowing a systematic cross between all strains of opposite mating type. We then determined whether each spore inherited the wild-type or the mutated allele by Sanger sequencing of the candidate gene.

Eight ancestral haploid segregants (4 *MAT α* , *lys2* and 4 *MATa*, *ura3*) were randomly isolated from the ancestral population. For the hydroxyurea environment, we probed individually beneficial *de novo* mutations in *RNR2* (Y169H) and *RNR4* (R34I), which reside on different chromosomes of the *S. cerevisiae* genome. The *RNR2* mutant was isolated from WAXNA F12 1 HU 3 (clone C3) and the *RNR4* mutant from WAXNA F12 2 HU 1 (clone C1) at $t = 32$ days. For rapamycin, three evolved clones isolated at $t = 32$ days were used: one clone with no identifiable driver from WAXNA F12 2 RM 2 (clone C1), a homozygous *FPR1* mutant (W66*) from WAXNA F12 2 RM 1 (clone C3); and a heterozygous *TOR1* mutant (W2038L) from WAXNA F12 1 RM 2 (clone C3). For the hydroxyurea experiment, 21 tetrads were taken for crossing (12 for *RNR2* and 9 for *RNR4*) resulting in 84 spores. For the rapamycin environment, 25 tetrads were used (1 without driver, 4 for *FPR1*, 20 for *TOR1*), resulting in 100 spores.

A genetic cross of size 48×48 in hydroxyurea yielded 2,304 hybrids, and 56×56 in rapamycin, giving 3,136 hybrids. We performed the genetic cross using the Singer RoToR HDA robot on YPDA plates. Subsequently, the hybrid populations were grown for two rounds on minimal medium to ensure colonies of solely diploid cells and avoid haploid leakage. A small number of crosses were not successful due to mating inefficiency or slow growth (56 in hydroxyurea and 654 in rapamycin), leaving a total of 2,248 and 2,482 hybrids, respectively. This was due to mistyping of the mating locus in one *FPR1* spore and three *TOR1* spores, which were excluded together with their derived hybrids. Phenotypic measurements of the crosses were carried out using the high-throughput method of yeast colony growth described in ‘Growth phenotyping’.

Luria-Delbrück fluctuation assay

We performed a fluctuation test to determine the rate of loss-of-heterozygosity (LOH) in different backgrounds, by following the loss of a heterozygous *URA3* marker that results in 5-FOA resistant colonies (Luria and Delbrück, 1943; Lang and Murray, 2008). In all strains tested the *URA3* gene was deleted from its native location in chromosome V and inserted in the *lys2* locus (*lys2::URA3*) in chromosome II (~470 kb) (Fig. 3B). This genotype is the same used in the crossing phase and therefore shared by all individuals in the population. Our system does not have dedicated markers to distinguish different mechanisms leading to LOH but instead gives an aggregate measurement of the total rate. The strains were first patched in URA dropout medium and then streaked for single colonies in plates with YPD or YPD supplemented with the drugs (HU at 10 mg ml^{-1} or RM at $0.025 \text{ } \mu\text{g ml}^{-1}$). Colonies were grown for 3 days at $30 \text{ }^\circ\text{C}$. Cells were resuspended in water and cell concentration was measured by flow cytometry to obtain a correct dilution factor in the subsequent plating. Cells from each replicate were plated in YPDA to determine total number of colony-forming units and 5-FOA (1 g l^{-1}) plates to count colonies that are *URA3* defective. We confirmed the loss of the *URA3* marker by diagnostic PCR. Four replicates for each experiment were used to determine the rate.

To ensure the absence of meiotic spores we inspected ~100 cells per sample. This control was introduced for two reasons. First, the NA parent is a very fast and efficient sporulator (Gerke et al., 2006). We observed the induction of meiosis even without the specific KAc environmental signal required in the laboratory strain S288C (and its derivatives) to initiate sporulation. Second, rapamycin has been shown to promote sporulation by modulating the nutrient sensing pathway (Zheng and Schreiber, 1997). We did not observe fully formed meiotic spores during this experiment, though we cannot exclude that meiotic events before the meiotic commitment point (e.g. double-strand breaks) may have occurred that could affect the LOH rate (Laureau et al., 2016).

We fitted the fluctuation data to a model of the Luria-Delbrück distribution. We determined the expected number of LOH events per culture m , such that LOH rate can be estimated by $\mu = \frac{m}{N}$, where N is the average number of cells per culture. In the control environment, we observed a rate $\mu = 9.8 \times 10^{-6}$ per cell per division in the WA background, consistent with previous reports (Barbera and Petes, 2006; Andersen et al., 2008). We observed a ten-fold higher rate in the NA background ($\mu = 3.24 \times 10^{-5}$) and the WAXNA F₁ hybrid had an intermediate rate ($\mu = 7.39 \times 10^{-6}$). These data indicate that LOH rates can vary between genetic backgrounds. There was a sharp increase of LOH rates when colonies were grown in hydroxyurea, irrespective of the background tested. This finding is consistent with previous studies in the laboratory strain S288C reporting that replication stress promotes recombinogenic DNA lesions (Barbera and Petes, 2006). We also observed a background-dependent increase in LOH rate in the presence of rapamycin, especially in the NA founder. Rapamycin has been reported to trigger sporulation (Zheng and Schreiber, 1997) and it is likely that the formation of double-strand breaks during meiosis can increase the LOH rate.

Growth phenotyping

To carry out phenotype measurements we used a high-resolution scanning platform, Scan-o-matic, to monitor growth in a 1536-colony design on solid agar medium (Zackrisson et al., 2015). Solid media plates designed for use with the Singer RoToR HDA robot (Singer Ltd) were used throughout the experiment. Casting was performed on a leveled surface, drying for ~ 1 day. We designed a randomized experimental layout by distributing genotypes of interest over 1,152 positions across each plate, keeping every fourth position for 384 controls used for removal of spatial bias. Controls were interleaved in the pre-culture step using a custom-made RoToR pinning program.

We recorded phenotypic measurements using high-quality desktop scanners (Epson Perfection V700 PHOTO scanners, Epson Corporation, UK) connected via USB to a standard desktop computer. Scanner power supplies were separately controlled by power managers (GEMBIRD EnerGenie PowerManager LAN, Gembird Ltd, Netherlands) that immediately shut down the scanner lamp between scans. Images were acquired using SANE (Scanner Access Now Easy). We performed transmissive scanning at 600 dpi using 8-bit grey scale, capturing four plates per image. Plates were fixed by custom-made acrylic glass fixtures. Orientation markers ensured exact software recognition of fixture position. Each fixture was calibrated by scanner using a calibration model that provided positions for each feature of that fixture, relative to its orientation markers. Pixel intensities were normalized and standardized across instruments using transmissive scale calibration targets (Kodak Professional Q-60 Color Input Target, Kodak Company, USA). Scanners were maintained in a 30 °C, high-humidity environment (incubation room) and kept covered in custom-made boxes during experiments to avoid light influx and minimize evaporation.

Experiments were run for 3 days and scans were continuously performed every 20 minutes. Each image stack was processed in a two-pass analysis. The first-pass was performed during image acquisition and was responsible for setting up the information needed for growth estimations. Positions in each image were matched to the fixed calibration model using the fixture orientation markers, allowing detection and annotation of plates and transmissive scale calibration strips. In the second-pass analysis, images were segmented to identify plate and transmissive scale calibration strip positions. The calibration strips were trimmed and the pixel intensities compared to the manufacturer's supplied values, such that normalized pixel values remained independent of fluctuations in scanner properties over time and space. The colonies were detected using a virtual grid across each plate based on pinning format, and the grid was adjusted for the intersections to match the centre of the features detected. At every intersection, each colony and the surrounding area were segmented to determine the local background and pixel intensities. Differences in pixel intensity were converted to population size estimates $n(t)$ by calibration to independent cell number estimates (spectrometer and FACS). Based on these, we obtained growth curves in physical units.

Raw measurements of population size were smoothed in a two-step procedure. First, a median filter identified and removed local spikes in each curve. Second, a Gaussian filter reduced the influence of remaining local noise. Since we expect a population to double in size during the average time taken to progress through the cell cycle, we use an exponential growth model defined as $n(t) = n(0) e^{\lambda t}$, where λ is the absolute growth rate. If the time that has passed is exactly the doubling time τ , it can be shown that within this time span the growth rate can be rewritten as $\lambda = \frac{\ln 2}{\tau}$. It follows that λ can then be estimated from the linear fit of any two log-transformed measurements of $n(t)$ in exponential phase, according to $\lambda = \frac{\ln n(t_f)/n(t_i)}{t_f - t_i}$. For quality control, the residuals of the model are then used to determine goodness-of-fit and to flag growth curves suspected to be of poor quality, which are visually inspected for artefacts. Rejection rates averaged approximately 0.3% across experiments.

To account for systematic errors caused by spatial variation within plates, we used an isogenic control at every fourth position. We defined a two-dimensional reference matrix for doubling time estimates of the 384 controls (on each 1,536 plate) to correct for structured spatial bias. Controls with extreme values were removed and the remaining control positions were used to interpolate a normalization surface. This surface was first smoothed

with a kernel filter to exclude any remaining noisy measurements, and then with a Gaussian smoothing to soften the contours of the landscape. For a colony measured at position ij , the absolute growth rate was rescaled by taking the log-transformed difference between the observed estimate and the growth of the normalization surface, i.e. the relative growth rate is then $\lambda_{ij} \rightarrow \log_2 \frac{\lambda_{ij}}{\lambda_{ij}^{\text{norm}}}$. To account for systematic bias between plates, the growth parameters were transformed by shifting the mean of the controls on each plate to match the mean of all plates in the experimental series.

Media composition

During the crossing phase, the cells were expanded and maintained in YPDA medium (2% glucose, 2% peptone, 1% yeast extract and 2% agar). WAXNA F₁/F₁₁ populations were sporulated in solid KAc medium (2% potassium acetate and 2% agar). WAXNA F₂/F₁₂ populations were then selected in minimal medium lacking uracil and lysine (0.67% of yeast nitrogen base (YNB), 2% glucose and 0.2% of dropout mix minus uracil and lysine). The selection phase of the experiments was carried out in YPDA medium supplemented with the drug. All selection experiments with drugs (as well as follow-ups) used media supplemented with hydroxyurea (HU) at 10 mg ml⁻¹ or rapamycin (RM) at 0.025 µg ml⁻¹, supplied by Sigma-Aldrich. The drug concentrations were chosen by serial dilution of dose levels in haploid and diploid WA and NA strains. We selected concentrations that maximized the differential growth between the two diploid parents by ten-fold in each environment (Fig. 4, C and D).

As part of the follow-up assays, we used antibiotic resistance as a selectable marker to engineer gene deletions and build hemizygous strains, plating in YPDA supplemented with the corresponding antibiotic ('[Engineered genetic constructs](#)'). We supplemented YPDA medium with nourseothricin (Nat) at 100 µg ml⁻¹, hygromycin B (Hyg) at 200 µg ml⁻¹ and G418 at 400 µg ml⁻¹. Transformations of reciprocal hemizygous strains also relied on *URA3* as a selectable marker and were plated in minimal medium lacking uracil (0.67% YNB, 2% glucose and 0.2% dropout mix minus uracil). The fluctuation assay was carried out in YPDA, or YPDA supplemented with the drug ('[Luria-Delbrück fluctuation assay](#)'). Colonies defective in the *URA3* allele were selected in 5-FOA plates (YPDA medium supplemented with 5-fluoroorotic acid at 1 g l⁻¹). In the genetic cross, the clones used were sporulated in solid KAc medium described above ('[Genetic cross](#)'). Haploid strains were derived from dissected spores and genotyped for their mating type, *URA3/LYS2* auxotrophies and known *de novo* mutations. Strains were crossed in YPDA and selected in minimal medium depleted of uracil and lysine. Growth phenotyping on solid medium was performed in Singer PlusPlates (Singer Ltd). Each plate was cast with 50 ml of Synthetic Complete medium, composed of 0.14% YNB, 0.5% ammonium sulphate, 0.077% Complete Supplement Mixture (CSM, ForMedium), 2% (w/v) glucose and pH buffered to 5.8 with 1% (w/v) succinic acid. The medium was supplemented with 20 g l⁻¹ of agar.

B. Theory and data analysis

Sequence analysis

Short-read sequences were aligned to the *S. cerevisiae* S288C reference genome ([Release R64-1-1](#), downloaded from the [Saccharomyces Genome Database](#) on February 5, 2011). Sequence alignment was carried out with [Stampy](#) v1.0.23 ([Lunter and Goodson, 2011](#)) and local realignment using [BWA](#) v0.7.12 ([Li and Durbin, 2009](#)). After removing PCR duplicates, the median genome-wide DNA coverage was 94× across whole-population samples, 23× across ancestral isolates and 30× across evolved isolates (ranging from 9× to 150×; first quartile 24× and third quartile 91×).

We detected single-nucleotide variants where the WA and NA parents differ, which comprises the background variation segregating in the cross (52,466 sites). We obtained allele counts on these loci using GATK UnifiedGenotyper v3.5-0-g36282e4 ([DePristo et al., 2011](#)). These counts were polarized to report WA alleles at each locus, as neither of the parents is the reference genome. The allele counts for segregating variants were first processed using the filterHD algorithm, which takes into account persistence along the genome due to linkage and allows for jumps in allele frequency if there are emerging subclones in the populations.

To detect *de novo* mutations we used three different algorithms: [GATK UnifiedGenotyper](#) v3.5-0-g36282e4 ([DePristo et al., 2011](#)), [Platypus](#) v0.7.9.1 ([Rimmer et al., 2014](#)) and [SAMtools](#) v1.2-10 ([Li, 2011](#)). We focused on single nucleotide polymorphisms (SNPs) and small insertions and deletions (indels). We first performed calling of both SNPs and indels for all ancestral isolates, evolved isolates and the parents. Using [BCFtools](#) ([Li, 2011](#)), we subtracted parental variation from all derived samples (ancestral and evolved). We further subtracted variation found in ancestral isolates from all evolved samples to account for segregating variation that was missed. We then required to see a given variant in more than six reads, be covered by more than ten reads and pass the default flags for the algorithms. For all isolates we further required that there is only

a single alternative allele. We then used GATK UnifiedGenotyper to get variants identified by at least two of the algorithms. For whole-population samples we did not require only a single alternate allele and we changed Platypus filtering to allow also ‘allele bias’ calls. To detect allele frequency changes over time, we only considered loci where the minimum variant allele count across time points was less than two and the maximum more than six reads. To avoid an increase of false positives in regions where genetic heterogeneity (e.g. variation in copy number) could cause difficulties in mixed samples we used more stringent filters than for isolate samples on mapping and base quality biases and goodness of fit. Finally, to increase our sensitivity of detection of putative *de novo* variants in recurrent target genes, we looked for mutations in *CTF8*, *RNR2*, *RNR4*, *FPR1* or *TOR1* that were only called by a single algorithm.

Genome-wide scan of pre-existing variants under selection

We observed patterns of selective sweeps when a ‘driver’ allele with a significant fitness advantage starts to gain in frequency due to the selective pressure applied (Fig. 1B and Fig. S2). This movement also causes allele frequency changes at nearby loci containing ‘passenger’ alleles that are genetically linked with the driver, in a process called genetic hitchhiking.

To discern drivers and passengers, we consider a model of a population evolving in a regime of strong selection, where there is a favored allele (driver) at locus i , and a set of linked passengers. We have previously developed a computational approach to analyse selection acting on pre-existing genetic variation that results from a cross (Illingworth et al., 2012). Genetic drift plays a negligible role for allele frequency changes in the experiment as the population size ($\sim 10^7$ cells) is much larger than its duration (~ 200 generations). Therefore, we can assume that the allele frequencies change deterministically and the remaining noise is due to sampling caused by finite sequencing depth.

A selective sweep is then well approximated by a model of the frequency q_i^{WA} of the WA allele at locus i which satisfies the logistic equation,

$$\frac{dq_i^{\text{WA}}}{dt} = \frac{\sigma}{2} q_i^{\text{WA}}(1 - q_i^{\text{WA}}). \quad (1)$$

The frequency of the NA allele at locus i is $q_i^{\text{NA}} = 1 - q_i^{\text{WA}}$. Here, the selection coefficient σ_i is the fitness difference $f_i^{\text{WA}} - f_i^{\text{NA}}$ between the alleles, and the pre-factor reflects a diploid population with additive selection. This growth model is a deterministic approximation to the stochastic evolution of $q_i(t)$, which is commonly described by the Wright-Fisher model with directional selection.

To account for the effects of linkage between mutations, we consider a model with two alleles possible at each locus, in which the driver mutation is at locus i and passengers at loci j . We refer to the two alleles at the i locus as $a \in \{\text{WA}, \text{NA}\}$, and the alleles at the j loci as $b \in \{\text{WA}, \text{NA}\}$.

According to our model, the dynamics of passenger alleles are fully specified by the motion of the local driver. The effect of the selected allele on existing variation at a passenger locus j is given by

$$q_j^b(t) = \sum_{a \in \{0,1\}} q_i^a(t) \frac{q_{ij}^{ab}(t_0)}{q_i^a(t_0)}, \quad \text{with } j \neq i \quad (2)$$

where the two-locus haplotype frequency is $q_{ij}^{ab}(t_0) = q_i^a(t_0)q_j^b(t_0) + (-1)^{a+b}D_{ij}$, and D_{ij} denotes linkage disequilibrium.

We note that due to short-read sequencing of a mixed population we cannot directly measure q_{ij}^{ab} or linkage disequilibrium, but we can parameterize D_{ij} in terms of the recombination which took place during the crossing phase. After N_c generations of sexual recombination, $D_{ij}(t) = (1 - \rho_{\text{tot}})^{N_c} D_{ij}(t_0)$, where the total recombination rate $\rho_{\text{tot}} = \rho \Delta_{ij}$ depends on the distance between the loci Δ_{ij} in base pairs (bp) and the local recombination rate ρ in units of $(\text{bp} \times \text{gen})^{-1}$.

Therefore for a given driver locus and a set of passengers the model is fully specified by the strength of selection, the pairwise linkage structure (or recombination landscape), and allele frequencies at both driver and passenger loci at $t=0$ days. Previously, we learned all these parameters via a maximum likelihood approach with a binomial noise model accounting for sequencing noise coupled with a search heuristic for proposing candidate driver locations.

Here we have made two extensions to this approach. Firstly, we utilize a recombination landscape inferred for this cross in a separate study to remove the need to estimate a local recombination rate from the allele frequency movement (Illingworth et al., 2013). Secondly, we use the posterior mean of the allele frequency at $t=0$, as obtained with the filterHD algorithm, to fix the initial condition. As a result, for each driver-passenger model we only need to learn the strength of selection and we can therefore systematically scan through each of the 52,466 segregating sites and test the alleles at each locus to be under selection. The resulting log-likelihood score is

compared to a null model where selection on the driver locus is set to zero. This null model corresponds to no frequency changes during the experiment (no parameters to be learned) and scoring the observations from different time points using $t = 0$ allele frequencies from filterHD.

We performed a systematic driver scan including passengers within variable window sizes ± 2 kb, 5 kb, 10 kb, 30 kb, 50 kb. Emerging subclones result in global allele frequency changes that supersede the local signal, which is the hallmark of selection acting on pre-existing variation. In consequence, we only considered time points when populations had not yet become clonal, up to $t = 4$ days. For each scan we selected the top 200 loci (out of 52,466) and then required that a given window was identified to be among the top scoring ones in at least two populations. The remaining windows were merged if their passenger loci overlapped. Finally, we required that the region was not identified among those scoring highly in the control environment.

The scan identified a region of interest for rapamycin resistance, found in chromosome VIII around 460 kb–490 kb as discussed in the main text. The signal is visible in all rapamycin populations but not in the control. However, we were not able to localize it fully due to a low recombination rate in this region and possibly also caused by the presence of multiple drivers. The top hits with different passenger window sizes show substructure in terms of peak location. Smaller windows contain multiple peaks, which then get merged to single peaks in larger windows. We note that theoretically the passenger window size should not matter provided the linkage model is good enough and there are no multiple drivers affecting the passenger dynamics. In summary, the region as a whole has strong support across populations to contain pre-existing variation where NA allele(s) are beneficial in rapamycin, albeit we cannot statistically map the signal more finely. From candidate genes in the region, we validated *CTF8* to have a resistance phenotype (see ‘[Genome-wide scan of pre-existing variants under selection](#)’). The region also contains *KOG1* (the gene has pre-existing missense variants in the population) which is part of the TOR pathway and so a plausible target of selection here. We did not find regions that replicated across all populations in hydroxyurea.

Reconstruction of subclonal composition

In the late stages of the selection experiment we identified global allele frequency changes of pre-existing, segregating variants caused by one or multiple *de novo* mutations (or a particularly favorable combination of the background variation itself) in clones that are under positive selection. During the selection phase, which is asexual, mutations in the genome of a cell are physically linked. Thus after a cell acquires a beneficial *de novo* mutation this can outweigh all its background variants, which become passengers (they may of course contribute to the fitness of that cell as well). At the genomic level, such an expanding subclone leaves a large imprint on the data at polymorphic sites, with long-range correlations reflecting the genotype of the cell hit by the beneficial *de novo* mutation. This movement with global, long-range correlations and sudden jumps corresponding to the expanding genotype is qualitatively different from the movement resulting from the localized sweep picture discussed in the previous section.

In this section, we describe how we extend and use the cloneHD algorithm (Fischer et al., 2014) to reconstruct the emerging subclone dynamics in a cell population. The cloneHD algorithm was developed to explain data from short-read DNA sequencing experiments of mixed cell populations (read depth and variant counts) under the following assumptions: (i) The cells evolve asexually (without recombination). This ensures that there are long-range correlations along the genome, which can, in principle, be reconstructed from short-read data. (ii) The population consists of a mixture of subclones, i.e. groups of genetically identical cells. The total number of subclones and their relative fractions in the population are unknown. The number of subclones, which can be reconstructed from real data, is small and depends on how different they are and what their population fractions are. (iii) Each subclone carries a unique copy number profile and genotype. Both of which are unknown. (iv) There is a distinct bulk component of the population which differs from the subclones, e.g. by having a different set of genotypes. Its fraction is also unknown. (v) When several samples are jointly analyzed, the same subclonal populations are assumed to be present in all samples. However, their frequencies in some of the samples can be zero.

Previously, cloneHD was used to explain subclonal heterogeneity found in human cancers. With a few extensions, this methodology can also be used for the yeast evolution experiment studied here. After the crossing phase, the populations evolve asexually under selective pressure. The rounds of crossing of the two original strains have produced a diverse pool of recombinants, where the genotype of each cell is – for all practical purposes – unique. This ancestral population of diploid cells is modeled here as the bulk component. Its allele frequency profile can be seen in Fig. 1B and Fig. S2.

At the later stages of the evolution, a small number of individual yeast cells start to outgrow the rest of the population, maybe due to a lucky combination of pre-existing variation or due to *de novo* mutations. These cells grow clonally to measurable fractions of the population and leave their fingerprint in the allele frequency profile genome wide. In the extreme case, a single cell grows clonally to take over the entire population and its individual genotype that can be directly observed in the sequencing data. In the general case, there will

be mixture of subclones and bulk population as described above. As an added complication, subclone copy number profiles need not be pure diploid.

This scenario is already covered in principle in the model underlying cloneHD (see esp. Section 4 in the Supporting Information of Fischer et al. (2014)). In the current study, the population is sequenced at several time points such that there are multiple related samples available for inference with cloneHD. For the read depth N_i^t at locus i and time point t , the emission probability is

$$N_i^t \sim \text{Pois} \left(N_i^t \mid M^t \langle c \rangle_i^t \right), \quad (3)$$

$$\text{with } \langle c \rangle_i^t \equiv c_0 (1 - F^t) + \sum_{j=1}^n c_{ij} f_j^t \quad (4)$$

where M^t is the mean sequencing depth per haploid DNA, c_{ij}^t is the total copy number of subclone j at locus i , c_0 is the total copy number of the reference compartment (2 for diploid) and f_j^t is the frequency of subclone j (with $F^t \equiv \sum_{j=1}^n f_j^t$).

The number of WA reads n_i^t determines the observed allele frequency q_i^t and is assumed to be binomially distributed

$$q_i^t \approx \frac{n_i^t}{N_i^t}, \quad \text{with } n_i^t \sim \text{Bin} (n_i^t \mid N_i^t, x_i^t) \quad (5)$$

$$\text{where } x_i^t \equiv \frac{\langle g \rangle_i^t}{\langle c \rangle_i^t}, \quad \text{with } \langle g \rangle_i^s \equiv q_i^{t_0} (1 - F^t) + \sum_{j=1}^n g_{ij} f_j^s \quad (6)$$

where g_{ij} is the genotype of subclone j at locus i and $q_i^{t_0}$ is the initial allele frequency spectrum. The only substantial difference to the situation in the cancer setup is that here the genotype of a particular subclone j is persistent across large regions of the yeast genome reflecting the haplotype structure resulting from the cross. In cancer, these correlations along the genome are missing since the above model is only applied to somatic point mutations which fall randomly on the available chromosomes. Altogether, the subclonal structure of the yeast cell populations can be reconstructed with cloneHD in **cna+snv** mode, where both the CNA and SNV data are modeled with persistence along the genome. The rest of the cloneHD workflow fully applies. First, the read depth and allele frequency data is analyzed with filterHD, thus finding a segmentation of both data tracks for all samples jointly (in later stages subclones are larger and the transition points become more prominent). This information and the initial allele frequency profile $q_i^{t_0}$ are provided to cloneHD together with the read depth and pre-existing variant allele data in **cna+snv** mode. The maximum likelihood set of subclonal genomes (including their copy number profiles and genotypes) and their cell fractions is then found by cloneHD at each time point. Figure S1 shows the general setup and the cloneHD reconstruction for simulated data in one population.

We assessed the ability of our algorithm to recover several features of interest from simulated jump-diffusion processes over a range of plausible parameters. For each parameter set, we simulate a 1 Mb region with $L = 10,000$ observations and 60 reads per locus on average, then compute maximum likelihood estimates using different numbers of subclones. Our choice of jump probability for simulated data is set to 4×10^{-5} per base. This reflects the size of linkage blocks with plausible recombination scenarios during crossing. The clones are added in a chosen background assuming the bulk has reached a steady profile. We would like to reconstruct three features: (i) the total number of subclones, (ii) their subclonal frequency, and (iii) obtain posterior estimates of subclonal genotypes.

The maximum-likelihood estimates of the subclonal fractions are approximately equal to the true values. The reconstruction is shown in Fig. S1B as a black solid line, which is the cloneHD solution for the mean posterior SNV emission rate. We can recapitulate the correct number of breakpoints and their location. The fidelity of our reconstruction to the true subclonal genotype is corroborated by the close correlation between our estimates from whole-population sequencing and the true genotypes derived from clonal isolates.

Subclonal dynamics

To ascertain the expansion of subclones throughout the experiment from whole-population sequencing, we determined the allele frequency of *de novo* mutations in WA, NA and WAXNA populations during the selection phase. We found that these mutations typically did not reach detectable frequency (i.e. between 1–5%) until more than 50 generations had passed, with steady increases thereafter (Figs. S3 and S4). Across populations, we found 66 point mutations spanning 41 unique loci by whole-population sequencing, out of which 50 fall onto

coding sequence. These loci contain 32 functional driver mutations: 4 in *RNR2*, 10 in *RNR4*, 11 in *FPR1*, and 7 in *TOR1*. This includes two tri-allelic loci: one corresponding to *FPR1* driver mutations W66* and W66S, and another to a SNP and an insertion in *FPR1*.

To reconstruct the subclonal composition of each WxNA population we used cloneHD, providing the jumps found by filterHD and the posterior mean allele frequencies of the ancestral population to act as a bulk component for the inference (see ‘[Reconstruction of subclonal composition](#)’). As visual inspection did not reveal clear copy number aberrations in the samples we used cloneHD in snv mode. For each population, we systematically tried 0–4 subclones and determined the total data likelihoods under each model. The number of subclones per population are summarized in Table S1, together with the time evolution of subclone frequencies in Fig. S4. We required a log-likelihood gain greater than 20,000 units for the inclusion of an additional subclone. This conservative cut-off only allows genome-wide signals to be associated with a subclone. This is necessary as the bulk component of the population can also change throughout the experiment. This means that, with a less conservative cut-off, the algorithm could introduce artifactual subclones with suitable genotypes to improve fits in regions where selection acts on the bulk (see ‘[Genome-wide scan of pre-existing variants under selection](#)’).

Adaptive mutations and genome instability

Overall, we identified 91 SNPs and indels in 173 ancestral haploid isolates and 140 point mutations in 44 evolved diploid isolates. We detected 82 SNPs and 1 indel across 22 evolved isolates in hydroxyurea (range 1–8 per isolate), containing 10 adaptive mutations in *RNR2* and 12 in *RNR4* (Figs. S5 and S6). There were 56 SNPs and 1 indel across 22 evolved isolates in rapamycin (range 0–6 per isolate), which contained 8 adaptive mutations in *FPR1* and 5 in *TOR1* (Table S2). 33 out of 36 mutations detected by whole-population sequencing across WxNA populations could be found in clonal isolates. All *de novo* driver mutations found by clone sequencing were confirmed by targeted Sanger sequencing.

Sequence analysis revealed that 3 out of 4 unique variants in *RNR2* (N151H, E154G and Y169H) and 2 out of 3 unique variants in *RNR4* (R34G/I) mapped to a conserved domain of the ribonucleotide-diphosphate reductase small chain. *FPR1* mutations occurred at W66, either introducing a premature stop codon or changing to serine. Previous studies indicate that the majority of non-synonymous changes in *FPR1* affect protein stability (Koser et al., 1993). Furthermore, the premature stop at W66 truncated the residue required for rapamycin binding (Y89). We observed clones carrying the W66* mutation selected multiple times from the same founder population indicating a pre-existent individual carrying a heterozygous mutation and independent LOH events that render the loss-of-function mutation homozygous (Fig. S6B). All five driver SNPs in *TOR1* (S1972I/R, W2038L/C and F2045L) mapped to the FKBP12-rapamycin-binding (FRB) domain, which is ~100 aa long, providing a mechanistic explanation of the drug resistance (Fig. S6A). Previous studies have found dominant mutations in S1972 and equivalent mutations in the mammalian TOR (mTOR) have a similar effect on drug binding. Substitutions at W2038 with a similar dominant effect are equivalent by homology to those previously described in *TOR2* (W2042) (Lorenz and Heitman, 1995).

Using background variants as markers, we could detect mis-segregation of chromosomes leading to loss-of-heterozygosity. The presence or absence of the WA or the NA allele provides a robust signal of heterozygosity or LOH that is not affected by sampling noise in coverage. We used cloneHD to genotype the sequenced isolate samples at segregating sites. We then grouped isolate sequences by subclone lineage, requiring at least 80% genotype similarity. In hydroxyurea, this resulted in 22 isolates stemming from 8 clonal backgrounds, with more than a single isolate each. In rapamycin, 22 isolates were assigned to 4 clonal backgrounds, with more than a single isolate each. For each clonal background, we inferred its ancestral genotype. In case of a locus with a unique genotype across all isolates this value was assigned to be the ancestral state. In all other cases the ancestral state was set to be heterozygous as lost alleles cannot be regained. We then annotated all the isolates from each clone for LOH events. In addition, we segmented the coverage depth as a function of genomic position with cloneHD and found instances of copy number gains ($2n > 3n$) in chromosomes VIII, IX and X in hydroxyurea and chromosome IX in rapamycin, as well as whole-genome copy loss ($2n > n$) in rapamycin. Figure S6 shows the inferred ancestral genotypes and the derived SNPs, indels, LOH events and copy number variants, grouped by population and clonal background.

To exemplify the interaction between pre-existing and *de novo* variation, inspection of *de novo* mutations in the WxNA F12 1 HU 3 population shows that one SNP in *RNR2* spans six isolates, being part of an expanding subclone (see Figs. S4 and S6A). These isolates have further diversified by acquiring passenger SNPs and indels, and undergoing LOH. As discussed in the main text clones C5 and C6 grow faster than the other four and have both a large LOH event in chromosome II that is not present in the other isolates, possibly providing the growth advantage. In the case of the WxNA F12 1 RM 1 population, isolate C1 is haploid genome-wide whereas isolate C3 from the same expanding clone is diploid with prevalent LOH. Both individuals have a homozygous driver mutation in *FPR1* as is required for resistance phenotype.

To determine the rate of LOH events, we counted the number of independent events within a chromosome

that have led to the gain or loss of an ancestral allele in the evolved isolate sequences. This estimate is challenging given the ancestral states contain both homozygous and heterozygous loci, so that the precise end points of individual LOH events are not clear. To obtain a lower bound, we counted whether any isolate had undergone LOH affecting ≥ 10 consecutive background variants, for each chromosome in each clone. We found 48 events in hydroxyurea and 24 events in rapamycin (0.38 per chromosome per clone). We excluded two haploid individuals from this counting as well as from the length distribution of homozygosity tracts in Fig. 3A. We detected two events of cross-contamination between populations, but sampled isolates from these populations are still independent samples from the corresponding clones and therefore valid for the LOH analysis. The contamination detected however means that those *de novo* mutations involved should not be counted to have arisen independently.

Population averaging vs. individual measurements

Here we describe how we measure growth properties of an ensemble of cells when you may be looking at a heterogeneous population and multiple subclones, i.e. several haplotypes may be present. With an ensemble method, we will typically measure the population average. However, since we found subclones co-existing, these may be found in states that are far from the population mean. Hence, we determined the intra-population growth rate of the populations at the start and the end of the selection phase (Fig. 2 and Fig. S7). For each population, we estimated the probability distribution $p(\lambda_k^t)$ of the growth rate λ at time t by sampling k isogenic individuals. With an ensemble of $k = 96$ individuals per time point we took $n = 32$ replicate measurements per individual. The replicates were measured in two independent runs, evenly distributed over 16 experimental plates which were initiated from a single pre-culture plate and run in 4 scanners, all in parallel.

We modeled the probability distribution of the data as a mixture model of normal distributions, $p(\lambda) = \sum_{k=1}^K \pi_k$. We can interpret the mixing coefficients as the bulk and multiple clonal components. We determined the fraction F^t of cells in the fitter, faster growth state by fitting $p(\lambda)$ to a mixture of two normal distributions, with five fitting parameters: the two means and variances, and the relative weights between them. In bimodal populations, the weights provide F^t and the estimates are in good agreement with the average of the two inflection points surrounding the trough between the bulk and the clonal subpopulations.

Validation of putative driver genes

To test candidate driver mutations, we measured the growth rate of engineered gene deletions described in ‘[Engineered genetic constructs](#)’ to confirm whether their knockouts are beneficial. We also measured the growth of hemizygous strains to test allelic differences in driver genes with pre-existing and newly acquired mutations. The engineered genetic constructs are listed in Table S4. We performed $n = 64$ replicate measurements of each construct in two independent runs, which were initiated from a single pre-culture plate, evenly distributed over 16 experimental plates and simultaneously run in 4 scanners. The growth rate of each of these strains λ_{bg} is shown in Figs. S9 and S10, labeled by genetic background b and genotype g .

We deleted one copy of *RNR2* in WA and NA diploids and sporulation of these strains resulted in tetrads with two viable spores and two unviable *rnr2* Δ mutants, indicating that this gene is essential in both backgrounds. *RNR2* is also essential in the laboratory S288C background. Furthermore, the heterozygous deletions of *RNR2* diploids show strong haploinsufficiency for hydroxyurea resistance (Fig. S9). In contrast to its interaction partner, *RNR4* is not essential in the laboratory background. However, deletion of this gene in diploid WA and NA backgrounds proved it to be essential in the WA background. The NA strain is viable after deletion, though with severe growth defects. Diploid hemizygous strains for *RNR4* deletions in both backgrounds show increased sensitivity due to dosage effects (Fig. S9).

FPR1 and *TOR1* are not essential genes and we performed deletions in both haploids and diploids. *FPR1* directly binds rapamycin inhibiting the TOR pathway and its deletion is highly resistant (Fig. S10). Deletion of one copy of *FPR1* does not increase the growth rate in rapamycin, indicating that both copies of the gene need to be inactivated to drive resistance. Consistently with this observation, all mutations observed in *FPR1* are homozygous (see ‘[Luria-Delbrück fluctuation assay](#)’ for mechanisms leading to homozygosity). Large colonies in the *FPR1* plating assay all acquired double-hit events (*de novo* SNP or indel plus LOH) that inactivated both functional copies of the gene (inset in Fig. S10). Estimates of the number of colonies for parent and hybrid backgrounds follow a similar trend to the estimates obtained with the fluctuation test. In contrast, *TOR1* deletion results in high sensitivity to rapamycin and a single deleted copy does not alter the drug response (Fig. S10).

Reciprocal hemizygosity tests in ancestral hybrids confirmed background-dependent effects in *CTF8*, with strong positive selection acting on the NA allele as predicted by our model of driver-passenger dynamics. *KOG1*, which is a component of the TOR signalling pathway, did not show any allelic differences, but deleting

either copy caused haploinsufficiency in rapamycin. No allelic differences were observed for *DEP1*, *INP54* and *YNR066C*, which are confirmed as passengers. We also deleted either the wild-type or the mutated allele of evolved mutant clones, generating pairs of clones identical throughout the genome except for the candidate driver mutation. The four genes harboring driver *de novo* mutations do not appear to show allelic differences between the two parental backgrounds as shown by the reciprocal hemizyosity test.

Background-averaged fitness effects

We carried out a genetic cross to reconstruct a fraction of the genotypes that a population can explore and examined the average mutational effect of beneficial variants in multiple genetic backgrounds. We isolated isogenic individuals from parents, ancestral and evolved populations. As described in ‘Genetic cross’, we sporulated these diploid cells and selected haploid segregants of each mating type (48 in hydroxyurea and 56 in rapamycin), parameterized by an index a or α . We crossed the *MATa* and *MAT α* versions to create hybrids. The cross forms a two-dimensional lattice that is conveniently parameterized by the set of lattice positions a , α .

We obtained a set of measurements for the growth rate λ of individuals, each of which has a unique combination of background genotype b , *de novo* genotype d , sampling time t and auxotrophy x . Every haploid genome being crossed is an independent background indexed by $b_{\{a,\alpha\}} = 1, 2, \dots, n_b$ ($n_b = 48$ in HU and $n_b = 56$ in RM, either a or α), such that reshuffled diploid hybrids are parameterized by $b_{a\alpha}$. Genetic backgrounds are sampled before the cross (parents), before selection starts at $t=0$ (ancestral) or after $t=32$ days (evolved), such that $t_{\{a,\alpha\}} = 1, 2, \dots, n_t$ ($n_t = 2$ for the parents; $n_t = 4$ at $t=0$; $n_t = 42$ in HU and $n_t = 46$ in RM at $t=32$). We denote *de novo* genotypes by $d_{\{a,\alpha\}} = 1, 2, \dots, n_d$ ($n_d = 12$ for *RNR2*; $n_d = 9$ for *RNR4*; $n_d = 1$ without driver; $n_d = 4$ for *FPR1*, $n_d = 20$ for *TOR1*). Haploid spores are auxotroph and segregate with the mating locus, such that $x_{\{a,\alpha\}} \in \{ura3-, lys2-\}$, whereas diploid hybrids do not have amino acid deficiencies. To estimate the measurement error, we carried out n_r replicate measurements of each unique spore ($n_r = 12$ in HU and $n_r = 6$ in RM) and of each hybrid genotype combination ($n_r = 3$). Replicates were initiated from the same pre-culture plate, evenly distributed over 32 plates that and run in 4 scanners, all in parallel.

The data matrix shows the fitness effect of every *de novo* genotype d at each background b sampled at time t , averaged over measurement replicates and measured relative to the ancestral population (Fig. S11). Based on these measurements, we observed that *de novo* mutations are beneficial, yet their association to genetic backgrounds have idiosyncratic effects. The effects of *de novo* mutations are mediated by background fitness as evidenced by the large phenotypic variance. Genetic crosses between different backgrounds need not give rise to a ‘symmetric’ phenotype, as we only enforce 2:2 segregation for the mating locus *MATa*/ α . Whilst background variants will co-segregate with the mating locus, *de novo* mutations need not.

To examine the mean effects of functional genotypes in hydroxyurea (*RNR2*, *RNR4*) or rapamycin (*FPR1*, *TOR1*), we calculated an ensemble average of the growth rate λ over pairs of backgrounds $b_{a\alpha}$ with different degrees of relatedness,

$$\langle \lambda^{td} \rangle_{a\alpha}^b = \frac{1}{n_b} \sum_{b=1}^{n_b} \lambda_{a\alpha}^{btd} \quad (7)$$

with $\langle \dots \rangle$ the mean over genetic backgrounds. We found that, on average, *RNR2*, *RNR4* and *TOR1* mutations are dominant and highly penetrant (Fig. 4D and F, and Fig. S12B and D). In contrast, *FPR1* is recessive and only increases fitness when the mutation is homozygous and carries a fitness cost (Fig. 4F and Fig. S12D, respectively).

We partitioned the variation in fitness contributed by background and *de novo* driver mutations using linear mixed models. To model genetic backgrounds containing beneficial mutations we need to describe how likely a phenotype is in the presence or absence of any mutation. We restricted our model to pairs of individuals that are not closely related to avoid spurious correlations by population structure, so we retained ancestral and evolved individuals and excluded the parents. We are interested in the aggregate effect across all mutations within a spore or hybrid rather than the effects of individual variants. As the data represents a finite sample from the distribution of all possible genetic backgrounds, the background contribution to the phenotype is naturally modeled as a random-effect term (i.e. individual genetic backgrounds are drawn at random from a population, and the variance of the underlying distribution is to be inferred). In addition, other systematic effects that potentially contribute to fitness are modeled as fixed-effect terms: (i) time t when the individual was sampled, i.e. at $t=0$ (ancestral) or $t=32$ days (evolved); (ii) *de novo* driver mutation status d of the individual, e.g. *FPR1* driver mutation in homozygous state; and (iii) auxotrophy, denoted by x , e.g. *ura3-* or *lys2-*. We used the R-package lme4 to implement four nested linear mixed models outlined below (Bates et al., 2015).

Model 1

We first considered a model where we only included the background without other effects. This means that the observed growth rate λ_b for a background b conditioned on the random effect taking a value β_b is distributed as

$$(\lambda_b | \mathcal{B} = \beta_b) \sim \mathcal{N}(\beta_0 + \beta_b x_b, \sigma_\epsilon^2), \quad (8)$$

where β_0 is a constant that all backgrounds get and needs to be inferred, σ_ϵ^2 represents measurement noise, x_b is an element from the model design matrix (here 1 for each b as they all are assigned a value). Finally, the background growth rate is distributed as $\mathcal{B} \sim \mathcal{N}(0, \Sigma^2)$, its variance Σ^2 is a model parameter to be inferred. We note that for each background b we have multiple measurement replicates of λ_b . Altogether, Model 1 has three modeling parameters, β_0 , Σ^2 and σ_ϵ^2 .

Models 2, 3 and 4

Model 2 includes the same factors as Model 1, but the time of sampling t is nested as a fixed effect. Model 3 also accounts for *de novo* driver mutation status denoted by d . In addition, Model 4 includes a fixed effect accounting for amino acid deficiencies (or auxotrophy), denoted by x . Altogether the growth rate λ_{btdx} , conditioned on the random effect taking a value β_b , is distributed as:

$$(\lambda_{btdx} | \mathcal{B} = \beta_b) \sim \mathcal{N}\left(\beta_0 + \underbrace{\beta_b x_b}_{\text{random}} + \underbrace{\beta_t x_t + \beta_d x_d + \beta_x x_x}_{\text{fixed}}, \sigma_\epsilon^2\right), \quad (9)$$

where $\beta_t, \beta_d, \beta_x$ are fixed-effect terms to be inferred and x_t, x_d, x_x are elements of the model design matrix. Compared to Model 1, Models 2, 3 and 4 have extra parameters β_t, β_d , and β_x . The number of free parameters depends on how many unique levels each factor contains, e.g. how many driver mutations are sampled in the experiment.

The likelihood for a data vector λ given the full model (Model 4) can then be written as

$$\begin{aligned} P(\lambda | \text{model}) &= P(\lambda | \beta_0, \beta_t, \beta_d, \beta_x, \Sigma^2, \sigma_\epsilon^2) \\ &= \prod_{\langle a, \alpha \rangle} \prod_{r=1}^{n_r} \int P(\lambda_{btdx} | \beta_b, \beta_0, \beta_t, \beta_d, \beta_x, \Sigma^2, \sigma_\epsilon^2) \times P(\beta_b | \Sigma^2) d\beta_b \end{aligned}$$

where the integrand is the product of the probability density given by Eq. 9 and the posterior distribution over the random effects.

Next, we applied all four models to the phenotypes of the genetic cross: a genetic cross based on hydroxyurea selection, measured in hydroxyurea and a control environment; and a genetic cross based on rapamycin selection, measured in rapamycin and a control environment, both for spores and hybrids. We fitted each model using restricted maximum likelihood with the R-package lme4 (Bates et al., 2015), summarized in Table S7. Using Akaike's Information Criterion (AIC) for model selection all conditions had a score supporting Model 4 apart for those selected and measured in hydroxyurea, where both spores and hybrids supported Model 3. We compared the fitted and observed values and in all cases the fits were good, as shown in Fig. S13 for Model 4.

We can assess the overall goodness-of-fit of the models by the proportion of variance explained. In particular, we would like to know the contribution of various model components to the overall fit, and to do so we obtain separate measures for the partial contributions of fixed and random effects (Gelman and Hill, 2006)

$$r^2 = \frac{\sigma_F^2 + \sigma_R^2}{\sigma_F^2 + \sigma_R^2 + \sigma_\epsilon^2}, \quad (10)$$

where σ_R^2 is the variance contribution by random effects, any incremental fixed effect contributes additively to the fixed-effect variance, s.t. $\sigma_F^2 = \text{Var}(\beta_t x_t + \beta_d x_d + \beta_x x_x)$, and r^2 represents the proportion of variance explained by the fixed and random effects combined. Dropping the σ_R^2 term from the numerator, we can evaluate r^2 and the fixed-effects variance r_F^2 for linear mixed models, as described in (Gelman and Hill, 2006), and estimate the background contribution to the variance by $r^2 - r_F^2$. Then to further delineate the fixed-effect variances to individual contributions, we used the simpler models and their estimated r_F^2 . The variance components shown in Fig. 4D have been constructed this way. We note that modeling the background component using fixed effects instead leads to a variance decomposition that is nearly identical to that with linear mixed models as described here. However, we note that modeling the background as a fixed effect leads to a large number of parameters (one extra parameter per background) and thus describing the background by random effects is a better model for the data.

V. ACKNOWLEDGEMENTS

We thank Agnès Llored, Jordi Tronchoni and Martin Zackrisson for technical help; Elizabeth Gibson for support with library preparation and sequencing; and Erik Garrison, Daniel Kunz, Leopold Parts, David Posada and Magda Reis for critical reading of the manuscript. We also thank participants of the program on Evolution of Drug Resistance held at the Kavli Institute for Theoretical Physics (University of California, Santa Barbara) for discussions. I.V.-G. is a recipient of a Wellcome Trust PhD fellowship and a Sanger Early Career Innovation Award. This research was supported by the Wellcome Trust to I.V.-G. (grant number WT097678) and to V.M. (grant number WT098051), by Fundación Ibercaja to I.V.-G., by ATIP-Avenir (CNRS/INSERM), Fondation ARC (grant number SFI20111203947), FP7-PEOPLE-2012-CIG (grant number 322035), the French National Research Agency (grant numbers ANR-13-BSV6-0006-01 and 11-LABX-0028-01), Cancéropôle PACA (AAP emergence) and DuPont Young Professor Award to G.L. F.S. was supported by ATIP-Avenir (CNRS/INSERM), Becas Chile, CONICYT/FONDECYT (grant number 3150156) and MN-FISB (grant number NC120043) postdoctoral fellowships. A.F. was supported by the German Research Foundation (grant number FI 1882/1-1), J.L. by Fondation ARC (grant number PDF20140601375), B.B. by La Ligue Contre le Cancer (grant number GB-MA-CD-11287) and J.H. by the French National Research Agency (grant number 11-LABX-0028-01).

Author Contributions

I.V.-G., J.W., V.M. and G.L. designed research; I.V.-G., F.S., J.L., A.F., B.B., J.H., A.B., E.A.P. and V.M. performed research; I.V.-G. and V.M. analyzed data; and I.V.-G., V.M. and G.L. wrote the paper.

References

- [1] E. Toprak et al. Evolutionary paths to antibiotic resistance under dynamically sustained drug selection. *Nature Genetics*, 44(1):101–105, 2012. doi: 10.1038/ng.1034.
- [2] A. Marusyk et al. Non-cell-autonomous driving of tumour growth supports sub-clonal heterogeneity. *Nature*, 514(7520):54–58, 2014. doi: 10.1038/nature13556.
- [3] N. Q. Balaban, J. Merrin, R. Chait, L. Kowalik and S. Leibler. Bacterial persistence as a phenotypic switch. *Science*, 305(5690):1622–1625, 2004. doi: 10.1126/science.1099390.
- [4] S. E. Luria and M. Delbrück. Mutations of bacteria from virus sensitivity to virus resistance. *Genetics*, 28(6):491–511, 1943. doi: 10.1038/nature10260.
- [5] J. E. Barrick and R. E. Lenski. Genome dynamics during experimental evolution. *Nature Rev. Genetics*, 14(12):827–839, 2013. doi: 10.1038/nrg3564.
- [6] L. Parts et al. Revealing the genetic structure of a trait by sequencing a population under selection. *Genome Res.*, 21(7):1131–1138, jul 2011. doi: 10.1101/gr.116731.110.
- [7] G. I. Lang et al. Pervasive genetic hitchhiking and clonal interference in forty evolving yeast populations. *Nature*, 500(7464):571–574, 2013. doi: 10.1038/nature12344.
- [8] S. F. Levy et al. Quantitative evolutionary dynamics using high-resolution lineage tracking. *Nature*, 519(7542):181–186, 2015. doi: 10.1038/nature14279.
- [9] B. C. Young et al. Evolutionary dynamics of *Staphylococcus aureus* during progression from carriage to disease. *Proc. Natl. Acad. Sci. U.S.A.*, 109(12):4550–4555, 2012. doi: 10.1073/pnas.1113219109.
- [10] T. D. Lieberman et al. Genetic variation of a bacterial pathogen within individuals with cystic fibrosis provides a record of selective pressures. *Nature Genetics*, 46(1):82–87, 2014. doi: 10.1038/ng.2848.
- [11] M. Gerlinger et al. Intratumor heterogeneity and branched evolution revealed by multiregion sequencing. *N. Engl. J. Med.*, 366(10):883–892, 2012. doi: 10.1056/NEJMoa1113205.
- [12] D. A. Landau et al. Evolution and impact of subclonal mutations in chronic lymphocytic leukemia. *Cell*, 152(4):714–726, 2013. doi: 10.1016/j.cell.2013.01.019.
- [13] P. Eirew et al. Dynamics of genomic clones in breast cancer patient xenografts at single-cell resolution. *Nature*, 518(7539):422–426, 2014. doi: 10.1038/nature13952.
- [14] G. I. Lang, D. Botstein and M. M. Desai. Genetic variation and the fate of beneficial mutations in asexual populations. *Genetics*, 188(3):647–661, 2011. doi: 10.1534/genetics.111.128942.
- [15] Y. O. Zhu, M. L. Siegal, D. W. Hall and D. A. Petrov. Precise estimates of mutation rate and spectrum in yeast. *Proc. Natl. Acad. Sci. U.S.A.*, 111(22):2310–2318, 2014. doi: 10.1073/pnas.1323011111.
- [16] C. J. R. Illingworth, L. Parts, S. Schiffels, G. Liti and V. Mustonen. Quantifying selection acting on a complex trait using allele frequency time series data. *Mol. Biol. Evol.*, 29(4):1187–1197, 2012. doi: 10.1093/molbev/msr289.
- [17] A. B. Parsons et al. Integration of chemical-genetic and genetic interaction data links bioactive compounds to cellular target pathways. *Nature Biotechnology*, 22(1):62–69, 2004. doi: 10.1038/nbt919.
- [18] A. Fischer, I. Vázquez-García, C. J. Illingworth and V. Mustonen. High-definition reconstruction of clonal composition in cancer. *Cell Rep.*, 7(5):1740–1752, 2014. doi: 10.1016/j.celrep.2014.04.055.

- [19] M. A. Barbera and T. D. Petes. Selection and analysis of spontaneous reciprocal mitotic cross-overs in *Saccharomyces cerevisiae*. *Proc. Natl. Acad. Sci. U.S.A.*, 103(34):12819–12824, 2006. doi: 10.1073/pnas.0605778103.
- [20] A. M. Selmecki et al. Polyploidy can drive rapid adaptation in yeast. *Nature*, 519(7543):349–352, 2015. doi: 10.1038/nature14187.
- [21] P. A. zur Wiesch, R. Kouyos, J. Engelstädter, R. R. Regoes and S. Bonhoeffer. Population biological principles of drug-resistance evolution in infectious diseases. *The Lancet infectious diseases*, 11(3):236–247, mar 2011. doi: 10.1016/S1473-3099(10)70264-4.
- [22] D. F. Jarosz and S. Lindquist. Hsp90 and environmental stress transform the adaptive value of natural genetic variation. *Science*, 330(6012):1820–1824, 2010. doi: 10.1126/science.1195487.
- [23] J.-F. Flot et al. Genomic evidence for ameiotic evolution in the bdelloid rotifer *Adineta vaga*. *Nature*, 500(7463):453–457, 2014. doi: 10.1038/nature12326.
- [24] W. Weir et al. Population genomics reveals the origin and asexual evolution of human infective trypanosomes. *eLife*, 5:1–14, 2016. doi: 10.7554/eLife.11473.
- [25] C. B. Ford et al. The evolution of drug resistance in clinical isolates of *Candida albicans*. *eLife*, 4:e00662, 2015. doi: 10.7554/eLife.00662.
- [26] P. J. Stephens et al. Massive genomic rearrangement acquired in a single catastrophic event during cancer development. *Cell*, 144(1):27–40, 2011. doi: 10.1016/j.cell.2010.11.055.
- [27] M. J. Sadhu, J. S. Bloom, L. Day and L. Kruglyak. CRISPR-directed mitotic recombination enables genetic mapping without crosses. *Science*, 352(6289):1–5, 2016. doi: 10.1126/science.aaf5124.
- [28] I. W. Dawes and I. D. Hardie. Selective killing of vegetative cells in sporulated yeast cultures by exposure to diethyl ether. *Mol. Gen. Genet.*, 131(4):281–289, 1974. doi: 10.1007/BF00264859.
- [29] L. M. Steinmetz et al. Dissecting the architecture of a quantitative trait locus in yeast. *Nature*, 416(6878):326–330, 2002. doi: 10.1038/416326a.
- [30] F. A. Cubillos et al. Assessing the complex architecture of polygenic traits in diverged yeast populations. *Mol. Ecol.*, 20(7):1401–1413, 2011. doi: 10.1111/j.1365-294X.2011.05005.x.
- [31] F. Salinas et al. The genetic basis of natural variation in oenological traits in *Saccharomyces cerevisiae*. *PLoS ONE*, 7(11):1–12, 2012. doi: 10.1371/journal.pone.0049640.
- [32] G. I. Lang and A. W. Murray. Estimating the per-base-pair mutation rate in the yeast *Saccharomyces cerevisiae*. *Genetics*, 178(1):67–82, 2008. doi: 10.1534/genetics.107.071506.
- [33] J. Gerke, K. Lorenz and B. Cohen. Genetic interactions between transcription factors cause natural variation in yeast. *Science*, 323(5913):498–501, 2006. doi: 10.1126/science.1166426.
- [34] X. F. Zheng and S. L. Schreiber. Target of rapamycin proteins and their kinase activities are required for meiosis. *Proc. Natl. Acad. Sci. U.S.A.*, 94(7):3070–3075, 1997. doi: 10.1073/pnas.94.7.3070.
- [35] R. Laureau et al. Extensive recombination of a yeast diploid hybrid through meiotic reversion. *PLoS Genetics*, 12(2):1–30, 2016. doi: 10.1371/journal.pgen.1005781.
- [36] M. P. Andersen, Z. W. Nelson, E. D. Hetrick and D. E. Gottschling. A genetic screen for increased loss of heterozygosity in *Saccharomyces cerevisiae*. *Genetics*, 179(3):1179–1195, 2008. doi: 10.1534/genetics.108.089250.
- [37] M. Zackrisson et al. Scan-o-matic: high-resolution microbial phenomics at a massive scale. *bioRxiv*, 2015.
- [38] G. Lunter and M. Goodson. Stampy: A statistical algorithm for sensitive and fast mapping of Illumina sequence reads. *Genome Res.*, 21(6):936–939, 2011. doi: 10.1101/gr.111120.110.
- [39] H. Li and R. Durbin. Fast and accurate short read alignment with Burrows-Wheeler transform. *Bioinformatics*, 25(14):1754–1760, 2009. doi: 10.1093/bioinformatics/btp324.
- [40] M. A. DePristo et al. A framework for variation discovery and genotyping using next-generation DNA sequencing data. *Nature Genetics*, 43(5):491–498, 2011. doi: 10.1038/ng.806.
- [41] A. Rimmer et al. Integrating mapping-, assembly- and haplotype-based approaches for calling variants in clinical sequencing applications. *Nature Genetics*, 46(8):912–918, 2014. doi: 10.1038/ng.3036.
- [42] H. Li. A statistical framework for SNP calling, mutation discovery, association mapping and population genetical parameter estimation from sequencing data. *Bioinformatics*, 27(21):2987–2993, 2011. doi: 10.1093/bioinformatics/btr509.
- [43] C. J. R. Illingworth, L. Parts, A. Bergström, G. Liti and V. Mustonen. Inferring genome-wide recombination landscapes from advanced intercross lines: application to yeast crosses. *PLoS ONE*, 8(5):1–10, 2013. doi: 10.1371/journal.pone.0062266.
- [44] P. L. Koser et al. The tyrosine89 residue of yeast FKBP12 is required for rapamycin binding. *Gene*, 129(2):159–165, 1993. doi: 10.1016/0378-1119(93)90264-4.
- [45] M. C. Lorenz and J. Heitman. TOR mutations confer rapamycin resistance by preventing interaction with FKBP12-rapamycin. *J. Biol. Chem.*, 270(46):27531–27537, 1995. doi: 10.1074/jbc.270.46.27531.
- [46] D. Bates, M. Maechler, B. M. Bolker and S. Walker. Fitting linear mixed-effects models using lme4. *J. Stat. Soft.*, 67(1):1–48, 2015. doi: 10.18637/jss.v067.i01.
- [47] A. Gelman and J. Hill. *Data analysis using regression and multilevel/hierarchical models*. Cambridge University Press, 2006. doi: 10.2277/0521867061.
- [48] W. McLaren et al. The Ensembl Variant Effect Predictor. *Genome Biol.*, 17(122):1–14, 2016. doi: 10.1101/042374.
- [49] G. Liti et al. Population genomics of domestic and wild yeasts. *Nature*, 458(7236):337–341, mar 2009. doi: 10.1038/nature07743.
- [50] P. D. Sniegowski, P. G. Dombrowski and E. Fingerman. *Saccharomyces cerevisiae* and *Saccharomyces paradoxus* coexist in a natural woodland site in North America and display different levels of reproductive isolation from European conspecifics. *FEMS Yeast Research*, 1(4):299–306, 2002. doi: 10.1016/S1567-1356(01)00043-5.

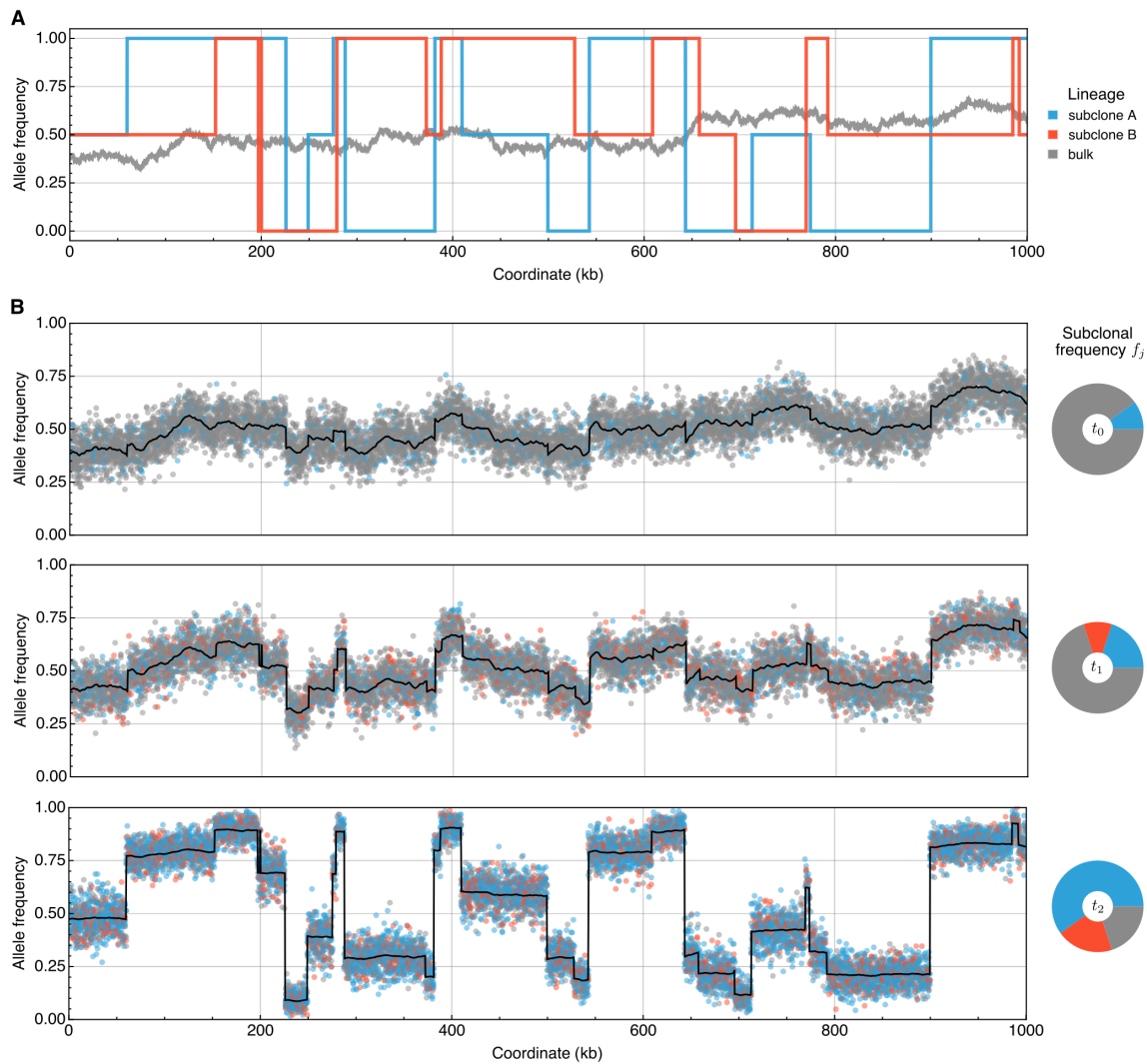


Figure S1: Subclonal reconstruction of a simulated example. Subclonal reconstruction using cloneHD for a simulated example of two macroscopic subclones. The physical locations of the segregating sites are represented along the x -axis and the y -axis shows the allele frequency at every locus. **(A)** The true allele frequency of the bulk (grey) and the true genotypes g_{ij} of two subclones (blue and red) at locus j for the simulated example. **(B)** Simulated jumps (subclones) and diffusion (bulk), in the presence of two subclones of size $f_j = (0.1, 0.0)$ at t_0 , $f_j = (0.2, 0.1)$ at t_1 and $f_j = (0.6, 0.2)$ at t_2 . The path along the genome is described by a mixture of the two, with jump probability $p = 4 \times 10^{-5} \text{ bp}^{-1}$, diffusion constant $\sigma = 5 \times 10^{-4}$, and binomial draws as emissions. The simulated observations are probabilistically color-coded according to the bulk fraction or each of the subclone fractions. The mean posterior estimate of the SNV emission in black solid line shows the accuracy of the reconstruction. The pie charts indicate the inferred bulk and subclone frequency estimates, \hat{f}_j .

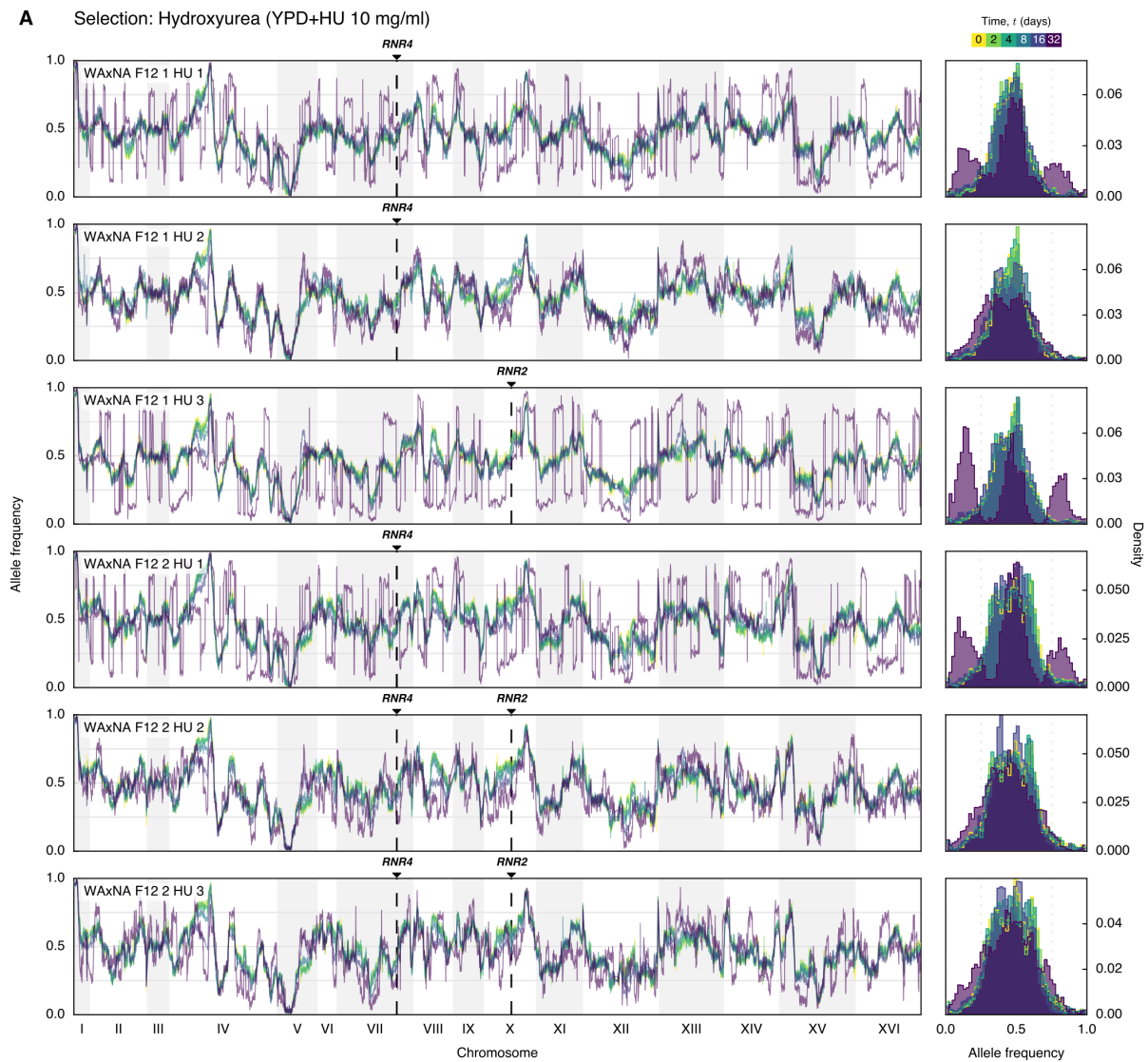


Figure S2: Genome-wide allele frequency changes of pre-existing variants. Time series of genome-wide frequencies, q_i^{WA} , of the WA allele after $t = (0, 2, 4, 8, 16, 32)$ days, measured by whole-population sequencing. From top to bottom, replicate populations were evolved in (A) hydroxyurea, (B) rapamycin and (C) a control environment. Allele frequencies are estimated from the mean posterior probability given by the filterHD algorithm. Left panels: Chromosomes are ordered along the x -axis; allele frequencies of 52,466 background variants are shown on the y -axis, colored by time point. Driver mutations are highlighted by arrows. Right panels: Changes in the allele frequency spectrum across time.

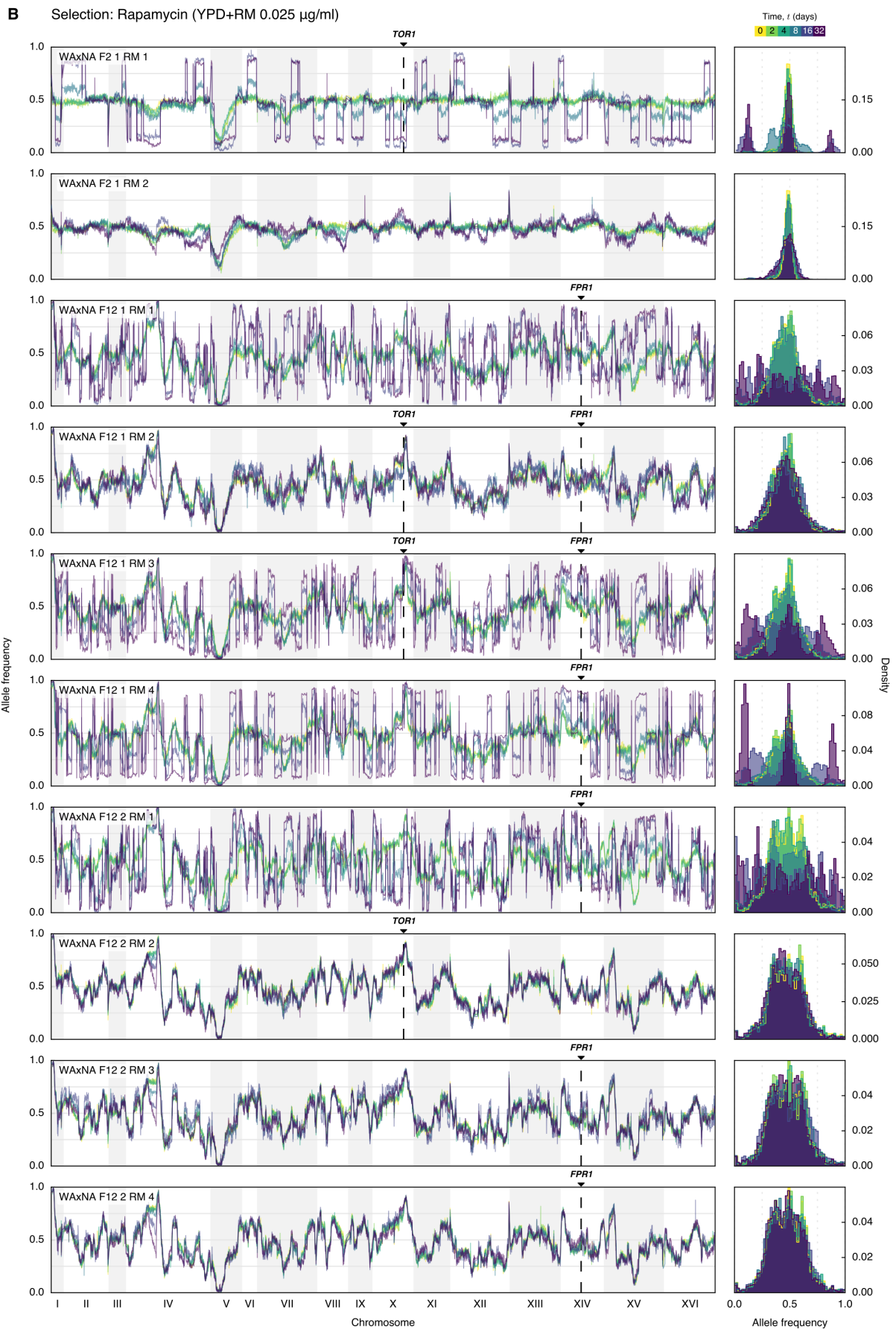


Figure S2: (continued)

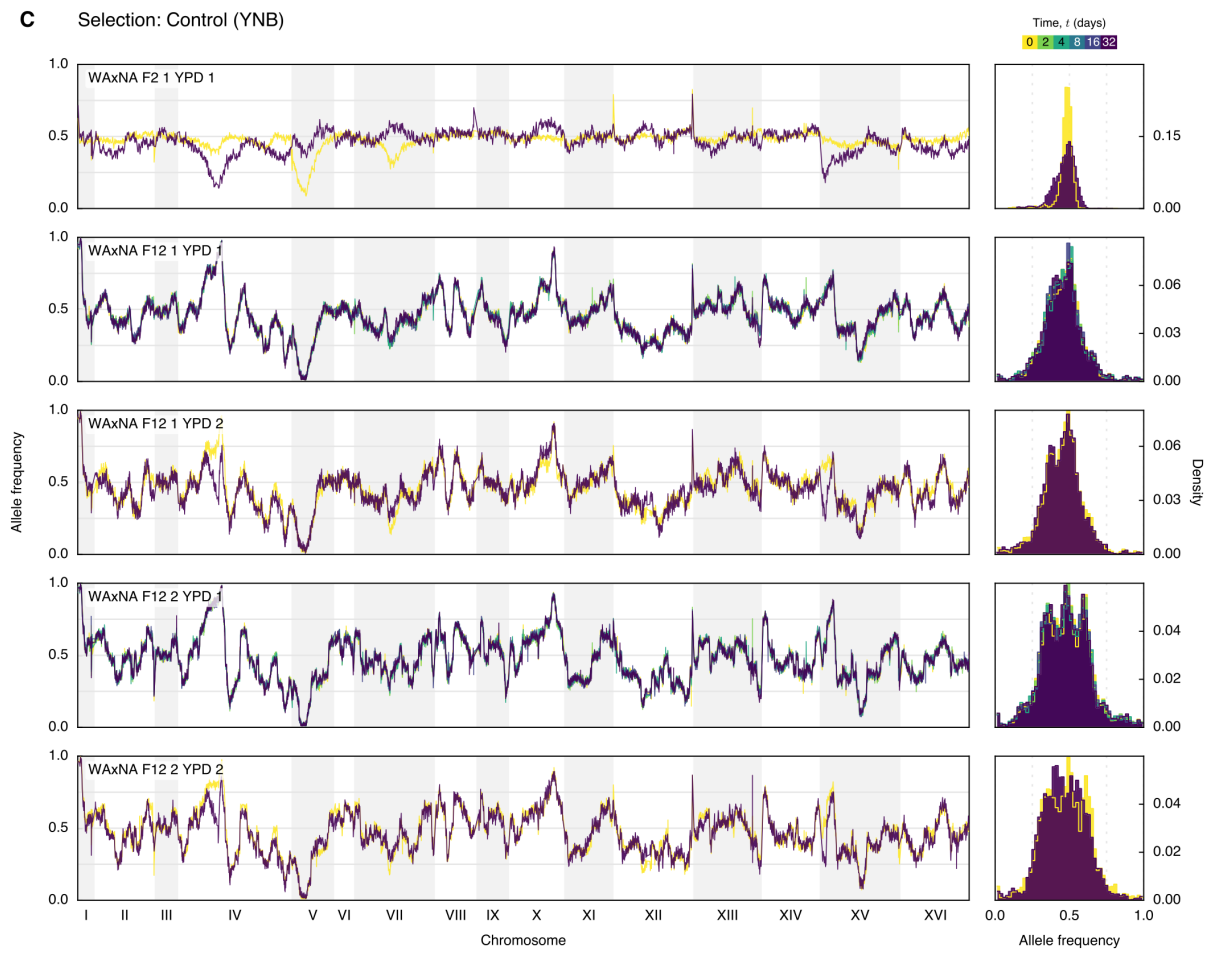


Figure S2: (continued)

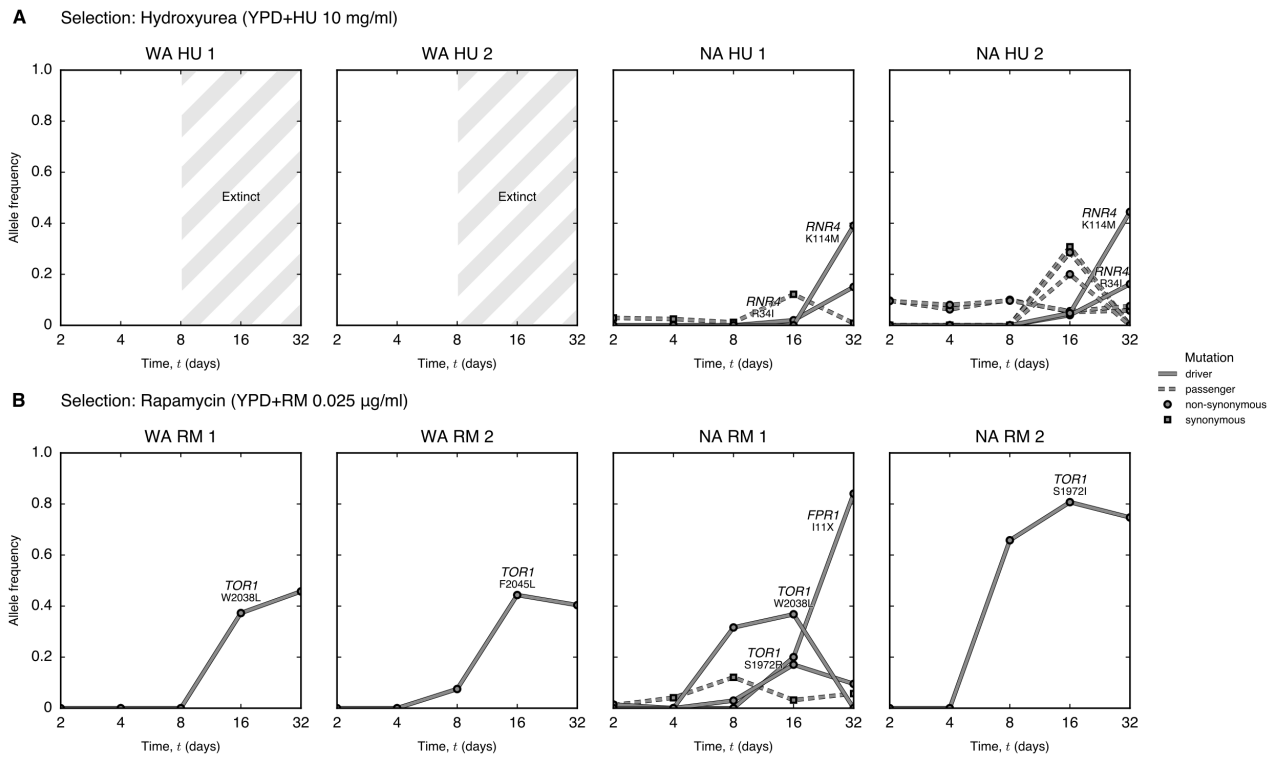


Figure S3: Subclonal dynamics in WA and NA populations. Subclonal dynamics in time for WA and NA founders evolved in (A) hydroxyurea and (B) rapamycin, measured by whole-population sequencing. WA founders evolved in hydroxyurea did not survive after 4 days. Driver mutations are solid lines and passenger mutations are dashed lines, colored by subclone assignment; circles and squares denote non-synonymous and synonymous mutations, respectively. No *de novo* mutations were detected in any of the control replicates in YPD.

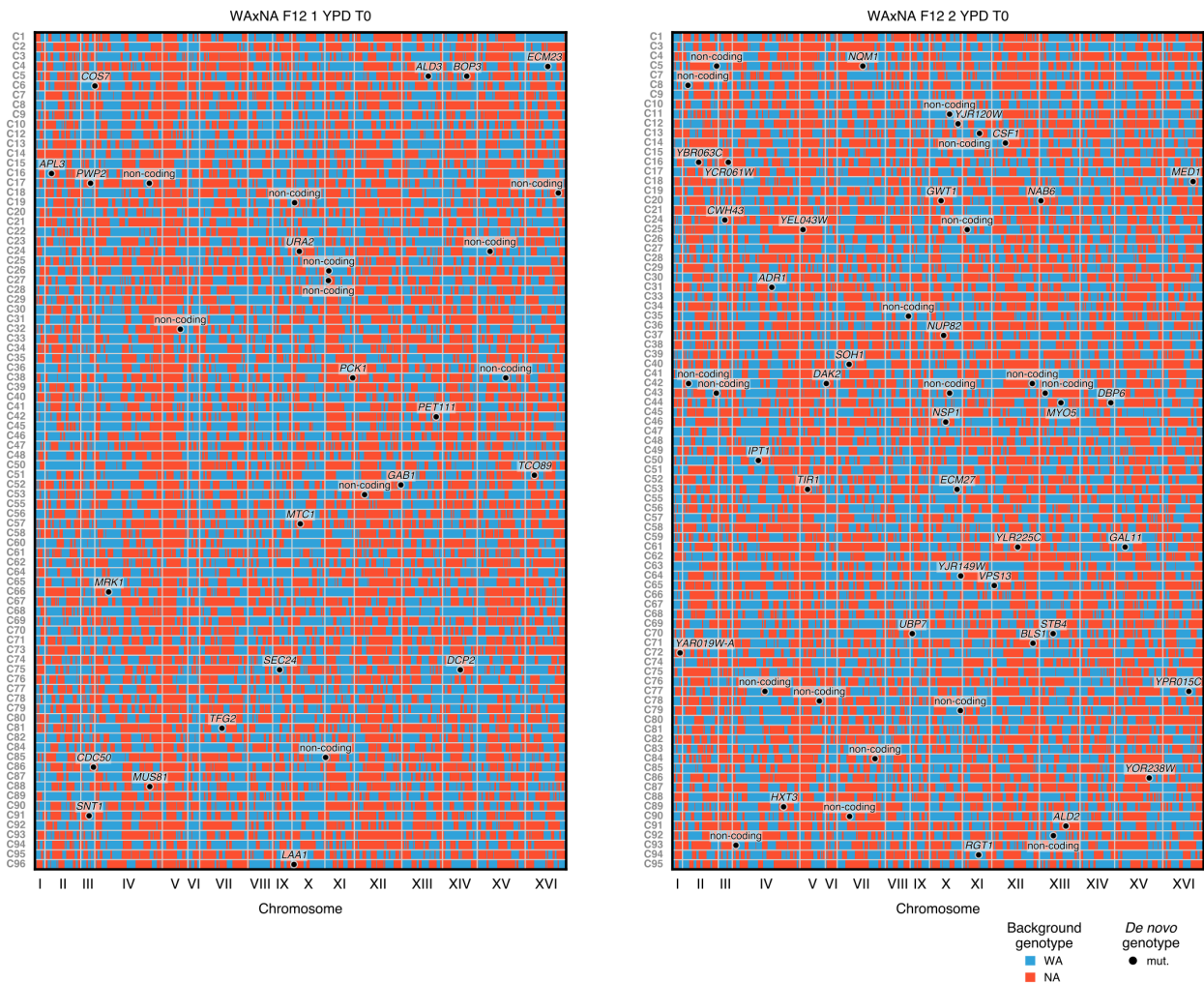


Figure S5: Genetic heterogeneity in sequences of ancestral clones. Sequences of ancestral haploid clones sampled from the WAXNA F₁₂ founder populations, which were obtained by bulk crossing between the WA and NA parents. Pre-existing and *de novo* SNPs and indels were detected by whole-genome sequencing in single-cell derived clones from ancestral populations at $t=0$ days. Chromosomes are shown on the x -axis; clone isolates are listed on the left. WA (in blue) and NA (in red) represent haploid genotypes. Individual cells with unique background genotypes carry private *de novo* SNPs and indels (circles).

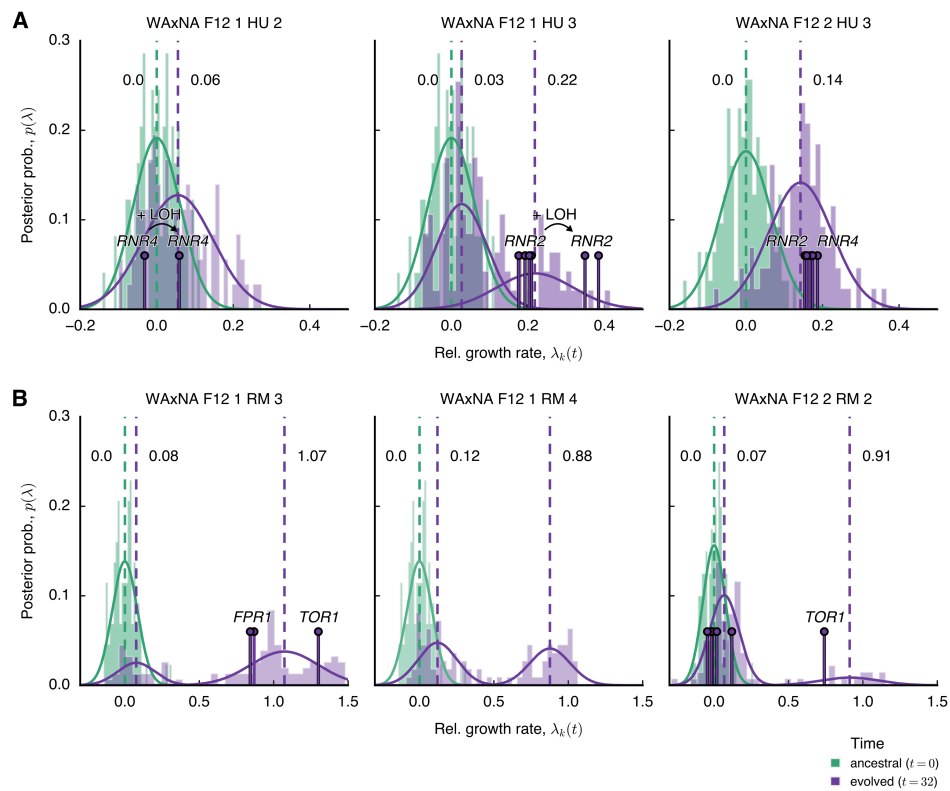


Figure S7: Variability in intra-population growth rate. Variability in intra-population growth rate, estimated by random sampling of 96 individuals at initial (0 days, green) and final time points (32 days, purple) for populations evolved in **(A)** hydroxyurea and **(B)** rapamycin. The mean growth rate λ per individual k is shown, averaging over $n = 32$ technical replicates per individual (see Fig. 2B and D). Using a Gaussian mixture model, we found the posterior probability of the mixture modes of the the best-fit mixture (solid lines). The posterior means of the distribution modes are indicated as dashed lines. The fitter individuals (pins) carry driver mutations, as determined by targeted sampling and sequencing.

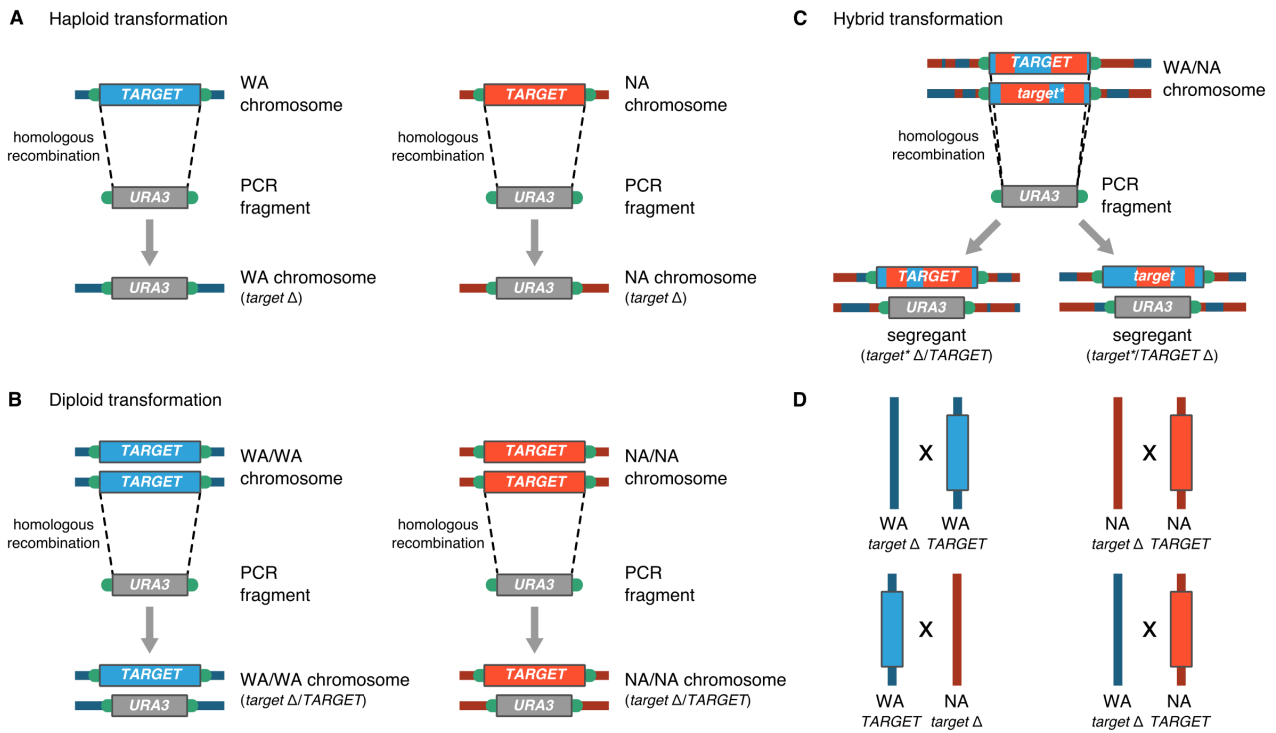


Figure S8: Strategy for strain construction. (A-C) Gene deletion was mediated by homologous recombination between the terminals of the PCR product and the corresponding genomic sequence where the gene to be deleted ('target') is encoded. Blue and red lines indicate WA and NA chromosomes, respectively. Flanking regions in green indicate two different homologous sequences targeted for recombination, which are 30-40 bp long in *S. cerevisiae*. Genes of interest were individually deleted in both WA and NA haploids, resulting in *rnr4*Δ, *fpr1*Δ and *tor1*Δ strains in both parental backgrounds. A similar strategy was used to delete genes in WA and NA homozygous diploids. *RNR2* and *RNR4* were only deleted in one allele while there is the wild-type gene remaining in the other allele. The primer sequences used are listed in Table S6. (C) Evolved segregants with *de novo* mutations were isolated from the WAxNA F₁₂ populations. Using the same strategy, *RNR2* or *TOR1* could be rid of either the wild-type allele or the mutated allele. (D) We crossed the strain constructed in (A), with the parental strain with wild-type gene, to obtain strains with deleted genes in WA, NA homozygous diploid and WA/NA hybrid.

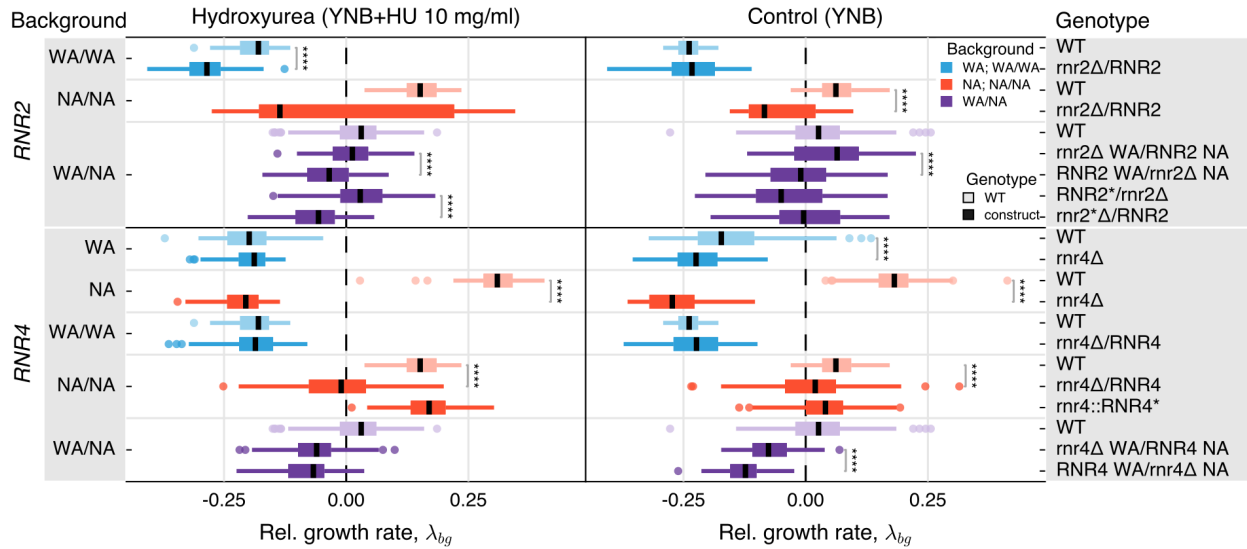


Figure S9: Validation tests for drivers in hydroxyurea. Validation tests for driver mutations in hydroxyurea, measured in YNB+HU (left panel) and YNB (right panel). Growth rate measurements, λ_{bg} , are shown for measurement replicates of each construct ($n = 64$) and grouped by candidate gene and by background of the construct, where the background b can be WA, NA (haploid); WA/WA, NA/NA (diploid); WA/NA (hybrid), and the genotype g can be wild-type for the gene, deleted or hemizygous. Medians and 25%/75% percentiles across groups are shown, with medians as horizontal lines and outliers highlighted. The color of each of the boxes reflects the background, with WA and WA/WA (blue), NA and NA/NA (red) and WA/NA (purple). Lighter shades indicate a wild-type (WT) control for that specific background and darker colors are the candidate strains. Using a non-parametric Wilcoxon rank-sum test, we compared deletion strains against their respective WT control and hemizygous strains against each other. Significance tests with $P < 10^{-4}$ are highlighted.

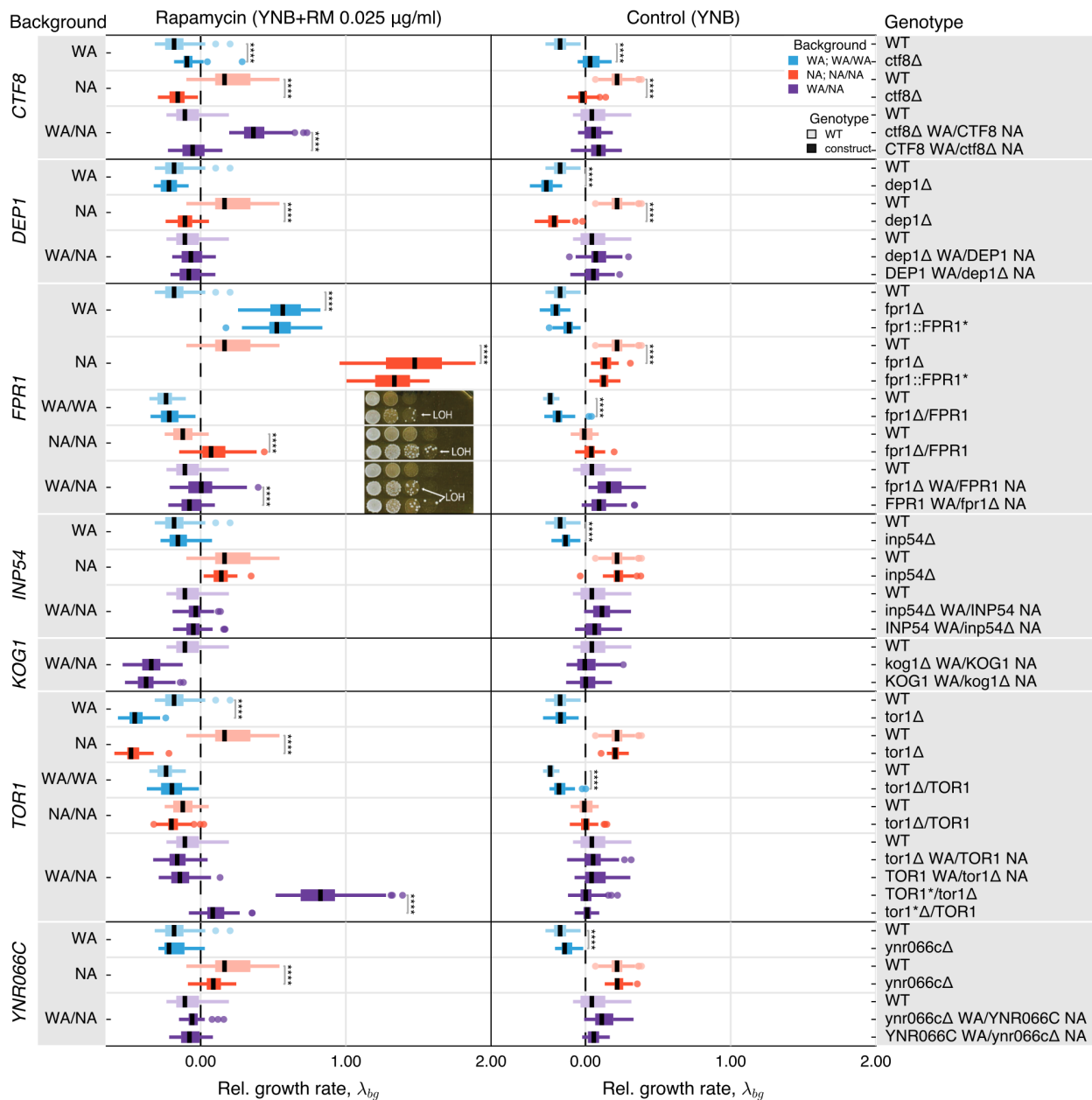


Figure S10: Validation tests for drivers in rapamycin. Validation tests for driver and passenger mutations in rapamycin, measured in YNB+RM (left panel) and YNB (right panel). Growth rate measurements, λ_{bg} , are shown for measurement replicates of each construct ($n = 64$) and grouped by candidate gene and by background of the construct, where the background b can be WA, NA (haploid); WA/WA, NA/NA (diploid); WA/NA (hybrid), and the genotype g can be wild-type for the gene, deleted or hemizygous. Medians and 25%/75% percentiles across groups are shown, with medians as horizontal lines and outliers highlighted. The color of each of the boxes reflects the background, with WA and WA/WA (blue), NA and NA/NA (red) and WA/NA (purple). Lighter shades indicate a wild-type (WT) control for that specific background and darker colors are the candidate strains. Using a non-parametric Wilcoxon rank-sum test, we compared deletion strains against their respective WT control and hemizygous strains against each other. Significance tests with $P < 10^{-4}$ are highlighted. Visual inspection of *FPR1* heterozygous deletions using a spot assay (inset) manifests the immediate loss of the wild-type allele by LOH – validated by colony Sanger sequencing.

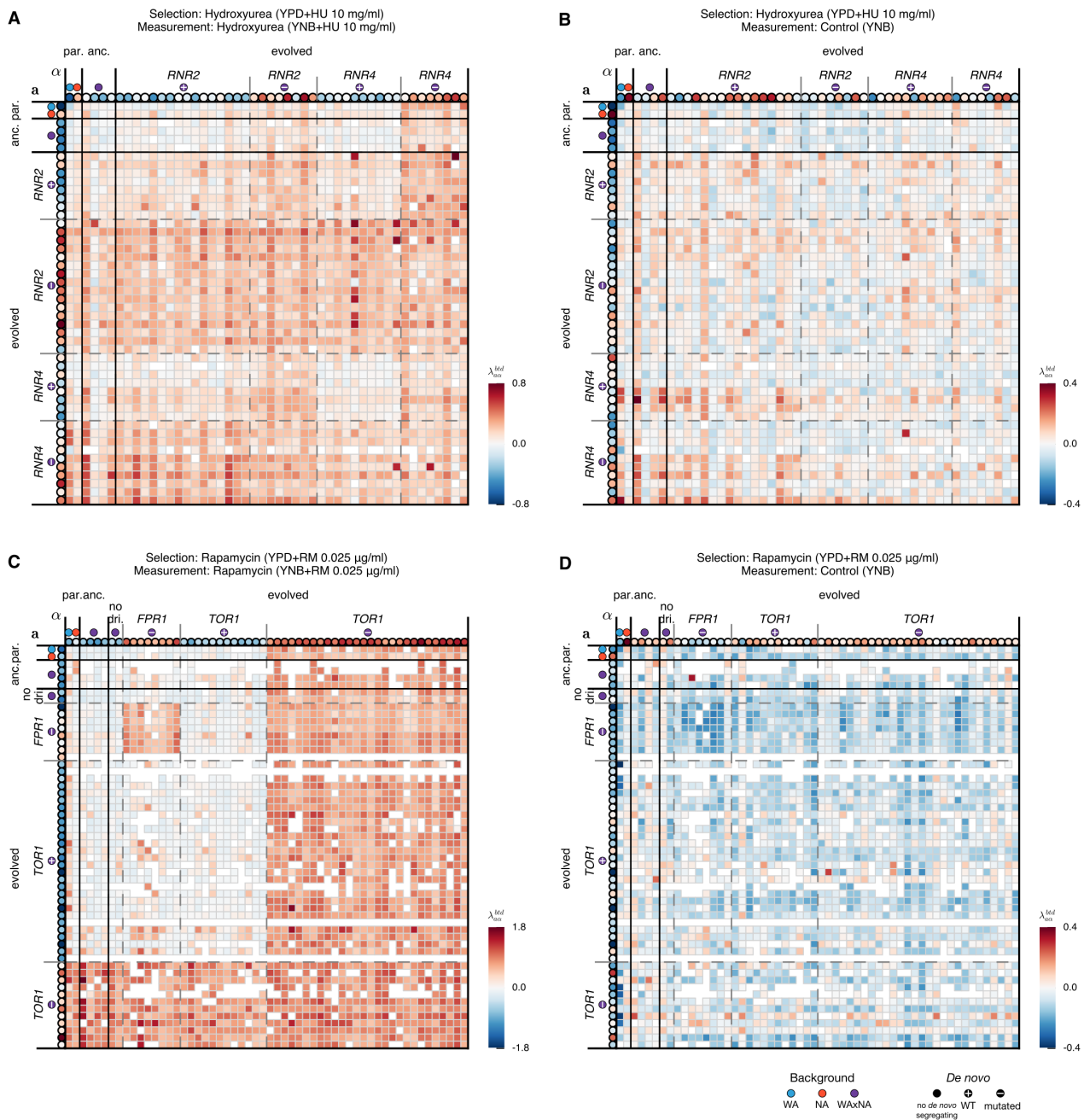


Figure S11: Fitness contribution of genetic background and *de novo* mutations. Given an ensemble of n_b unique genetic backgrounds ($n_b = 48$ in hydroxyurea and $n_b = 56$ in rapamycin), we constructed a matrix of size $n_b \times n_b$ where every unique haploid background is crossed against itself and all other haploid backgrounds, and the two must be of opposite mating type ($MATa$ or $MAT\alpha$). Each matrix element is labeled by background genotype, b ; *de novo* genotype, d ; time, t ; and auxotrophy, x . Measurements of relative growth rates of spores $\lambda_{\{a,\alpha\}}^{bt}$ and hybrids $\lambda_{a\alpha}^{bt}$ are shown, normalized with respect to the ancestral WAXNA crosses. Measurements are taken in (A) YNB+HU 10 mg ml⁻¹ and (B) YNB; (C) YNB+RM 0.025 μ g ml⁻¹ and (D) YNB, respectively. The color scale for all matrices to the right of each panel indicates the relative fold-change with respect to the ancestral WAXNA crosses. White boxes indicate missing data due to mating inefficiency and slow growth.

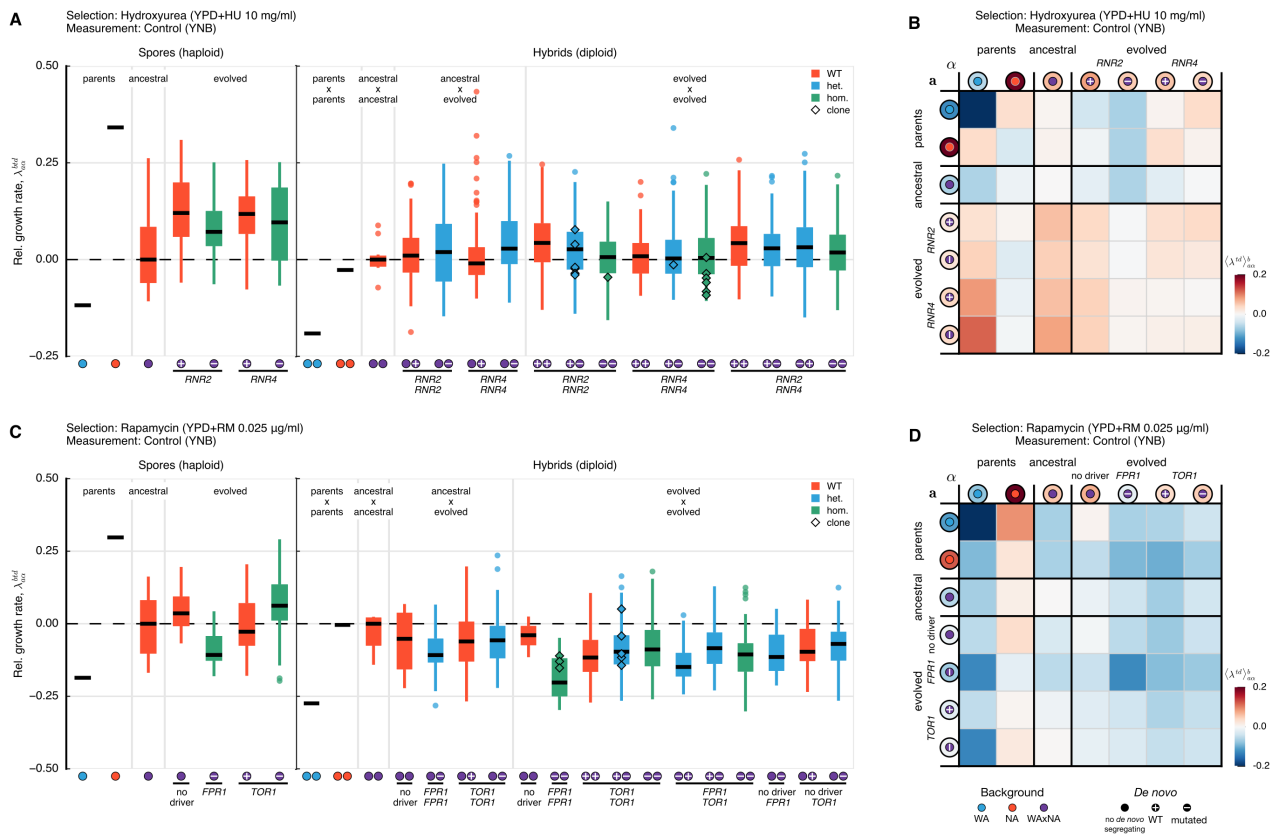


Figure S12: Ensemble average of fitness effects over genetic backgrounds. (A and C) Relative growth rate, λ , measured in a control environment (YNB) for cells selected in (A) hydroxyurea and (C) rapamycin. Measurements are normalized with respect to the ancestral population for multiple combinations (background genotype, b ; *de novo* genotype, d ; sampling time during selection, t ; auxotrophy, x) and averaged over measurement replicates. Medians and 25%/75% percentiles across groups are shown, with medians as horizontal lines and colored by *de novo* genotype [wild-type $+/+$ (red); heterozygote $+/-$ (blue); homozygote $-/-$ (green)]. Outliers (circles) and isolated, selected clones with matching genotypes (diamonds) are highlighted. (B and D) Ensemble average of the growth rate of spores, $\langle \lambda^{td} \rangle_{a,\alpha}^b$, and hybrids, $\langle \lambda^{td} \rangle_{a,\alpha}^b$, over genetic backgrounds. The color scale for all matrices to the right of each panel indicates the relative fold-change with respect to the ancestral WxNA crosses.

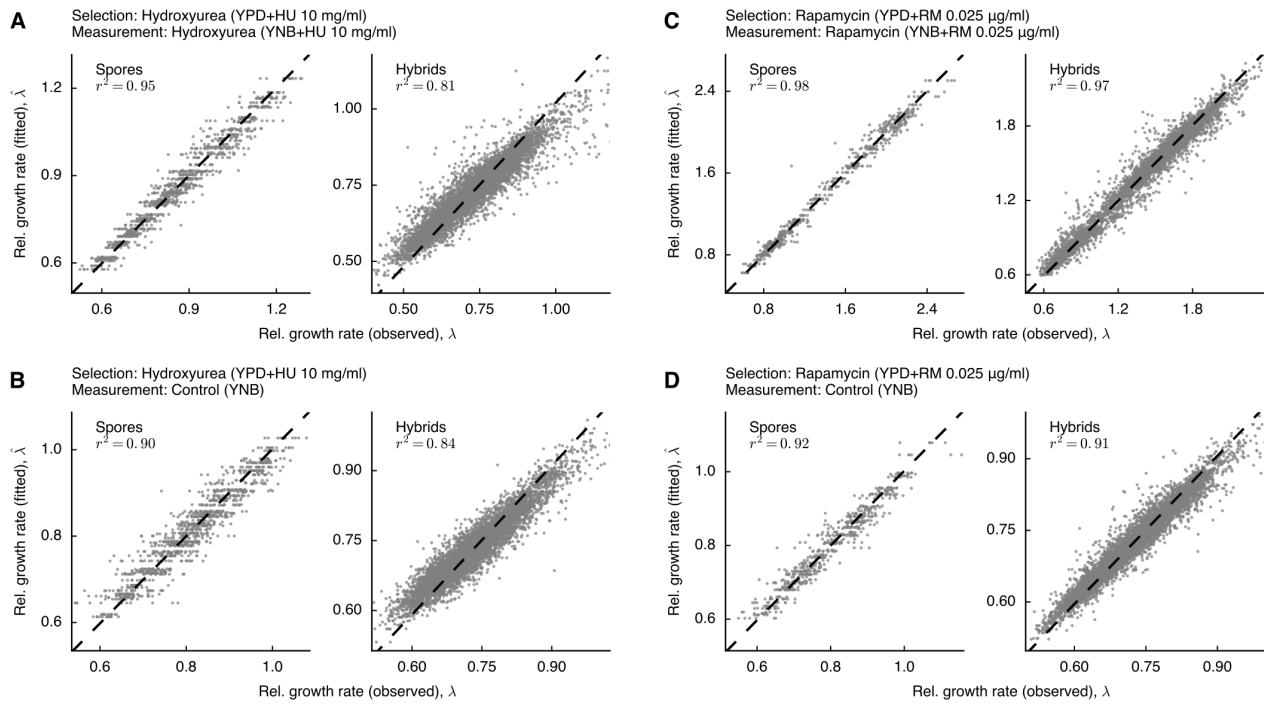


Figure S13: Hierarchical analysis of variance in the genetic cross using linear mixed models. We model the growth rate of spores $\lambda_{\{a,\alpha\}}^{btd}$ and hybrids $\lambda_{a\alpha}^{btd}$ as a function of background genotype b , *de novo* genotype d , sampling time during selection t , and auxotrophy x . Relative growth rates are accurately fitted by this model (Model 4). Model fits are summarized in Table S7. Measurements are taken in YNB+HU 10 mg ml⁻¹ and YNB only for populations selected in hydroxyurea (A and B); YNB+RM 0.025 µg ml⁻¹ and YNB only for populations selected in rapamycin (C and D). The scatter shows a set of measurements λ (x -axis) against the fitted rates $\hat{\lambda}$ (y -axis). The total variance explained, r^2 , is separately computed for spores and hybrids by environment.

Table S1: Summary of populations and clonal isolates analyzed by whole-genome sequencing in this study. The best-fit number of subclones N_c as estimated by cloneHD are shown together with the total clonal fraction, $F^t = \sum_{j=1}^n f_j^t$, after 32 days of selection. Per population, the union set of driver mutations found by whole-population and clone genome sequencing is shown. The genotypes of driver mutations found in clonal isolates were validated by Sanger sequencing (labeled by §). WA/WA populations in hydroxyurea did not survive beyond 4 days of selection (labeled by †).

Time	Background	Cross		Selection		Clonality		Drivers	
		Gen.	Rep.	Environment	Rep.	Isolates	N_c		F^t
0 days	WA/WA	–	–	–	–	–	–		
	NA/NA	–	–	–	–	–	–		
	WAxNA	F ₁₂	1	–	–	C1–C96	–	–	
2–32 days	WA/WA	–	–	YPD+HU	1†	–	–	–	
					2†	–	–	–	
	NA/NA	–	–	YPD+HU	1	–	–	–	<i>TOR1</i> W2038L [§]
					2	–	–	–	<i>TOR1</i> F2045L [§]
	WAxNA	F ₂	1	YPD+RM	1	–	2	0.74	<i>RNR4</i> R34I [§] , K114M [§]
					2	–	1	0.10	<i>RNR4</i> R34I [§] , K114M [§]
	WAxNA	F ₁₂	1	YPD+HU	1	–	0	–	<i>FPR1</i> K11fs [§] ; <i>TOR1</i> S1972R, W2038L [§]
					2	–	–	–	<i>FPR1</i> M11I [§] ; <i>TOR1</i> S1972I [§]
					3	–	–	–	<i>TOR1</i> W2038L
					1	–	–	–	
					2	–	–	–	
					3	C1–C2	2	0.58	<i>RNR4</i> R34G [§] , R34I [§]
					2	C1–C2	1	0.20	<i>RNR4</i> R34I [§]
					3	C1–C6	2	0.65	<i>RNR2</i> Y169H [§]
					1	C1–C3	3	0.85	<i>CTF8</i> ^{NA} , <i>FPR1</i> W66* [§] , W66S
					2	C1–C6	2	0.20	<i>CTF8</i> ^{NA} , <i>FPR1</i> W66S;
					3	C1–C3	2	0.72	<i>TOR1</i> W2038L [§]
					4	–	2	0.81	<i>CTF8</i> ^{NA} , <i>FPR1</i> W66* [§] ;
					1	–	0	–	<i>TOR1</i> S1972I
					2	–	0	–	<i>CTF8</i> ^{NA} , <i>FPR1</i> W66* [§]
	WAxNA	2	–	YPD+HU	1	C1–C2	2	0.63	<i>CTF8</i> ^{NA} , <i>FPR1</i> W66* [§] , W66S
					2	C1–C4	2	0.32	<i>RNR4</i> R34G [§] , R34I [§]
					3	C1–C6	2	0.34	<i>RNR2</i> N151H, T206I [§] ; <i>RNR4</i> R34I [§]
					1	C1–C3	4	0.93	<i>RNR2</i> E154G [§] ; <i>RNR4</i> R34I [§]
					2	C1–C6	1	0.10	<i>CTF8</i> ^{NA} , <i>FPR1</i> W66S, W66* [§]
					3	C1	1	0.10	<i>CTF8</i> ^{NA} , <i>TOR1</i> W2038C [§]
WAxNA	–	–	YPD	4	–	1	0.11	<i>CTF8</i> ^{NA} , <i>FPR1</i> S102R	
				1	–	0	–		
WAxNA	–	–	YPD	1	–	0	–		
				2	–	0	–		

Table S2: Summary of unique SNPs and indels found to be drivers in hydroxyurea (*RNR2*, *RNR4*) and rapamycin (*CTF8*, *FPR1*, *TOR1*). Nucleotide and protein substitutions show the wild-type and mutated alleles. Nucleotides gained or lost are underlined. The functional impact of the mutations has been characterized using the Ensembl Variant Effect Predictor [48].

Gene	Chr	Position	Strand	Nucleotide		Protein		Effect	Count
				Position	Substitution	Position	Substitution		
<i>CTF8</i>	VIII	486462	-	170	C(WA)>A(NA)	57	G>V	missense	-
		486568	-	64	T(WA)>C(NA)	22	T>A	missense	-
<i>FPR1</i>	XIV	371920	-	306-307	<u>T>TTG</u>	102-103	ST>S*	frameshift (stop codon gained)	1
		371921	-	306	A>T	102	S>R	missense	2
		372030	-	197	C>G	66	W>S	missense	3
		372030	-	197	C>T	66	W>*	nonsense (stop codon gained)	4
		372195	-	28-31	<u>ATTTT>ATTT</u>	10-11	KI>K*	frameshift (stop codon gained)	1
		372224	-	3	C>A	1	M>I	nonsense (start codon lost)	1
<i>RNR2</i>	X	392854	+	451	A>C	151	N>H	missense	1
		392864	+	461	A>G	154	E>G	missense	1
		392908	+	505	T>C	169	Y>H	missense	1
		393020	+	617	C>T	206	T>I	missense	1
<i>RNR4</i>	VII	855961	-	341	T>A	114	K>M	missense	2
		856201	-	101	C>A	34	R>I	missense	7
		856202	-	100	T>C	34	R>G	missense	2
<i>TOR1</i>	X	564757	+	5343-5345	<u>ATGA>A</u>	1781-1782	DD>D	in-frame deletion	1
		565330	+	5915	G>T	1972	S>I	missense	2
		565331	+	5916	C>A	1972	S>R	missense	1
		565528	+	6113	G>T	2038	W>L	missense	4
		565529	+	6114	G>C	2038	W>C	missense	1
		565550	+	6135	C>A	2045	F>L	missense	1

Table S3: Glossary of wild strains used in this study, including derivative strains. ^aIsolated in West Africa (pre-1914) by A. Guilliermond from bili wine from *Osbeckia grandiflora* [49]. ^bIsolated in Pennsylvania (1999) by P. Sniegowski from soil beneath *Quercus alba* [50].

Background	ID	Derived from	Genotype
WA	DBVPG6044	Wild isolate ^a	
	CC402	DBVPG6044	<i>MATa</i> , <i>ura3::KanMX</i> , <i>ho::HygMX</i>
	CC406	DBVPG6044	<i>MATα</i> , <i>ura3::KanMX</i> , <i>lys2::URA3</i> , <i>ho::HygMX</i>
	FS174	DBVPG6044	<i>MATα</i> , <i>ura3::KanMX</i> , <i>ho::NatMX</i>
	YGL1001	DBVPG6044	<i>MATa/α</i> , <i>ura3Δ0</i> ; <i>ura3Δ0</i> ; <i>leu2Δ0</i> ; <i>leu2Δ0</i> ; <i>lys2Δ0</i> ; <i>met15Δ0</i>
WA/WA	CC426	CC402 × CC406	<i>MATa/α</i> , <i>ura3::KanMX/ura3::KanMX</i> , <i>ho::HygMX/ho::HygMX</i> , <i>LYS2/lys2::URA3</i>
NA	YPS128	Wild isolate ^b	
	CC403	YPS128	<i>MATa</i> , <i>ura3::KanMX</i> , <i>ho::HygMX</i>
	CC407	YPS128	<i>MATα</i> , <i>ura3::KanMX</i> , <i>lys2::URA3</i> , <i>ho::HygMX</i>
	FS173	YPS128	<i>MATα</i> , <i>ura3::KanMX</i> , <i>ho::NatMX</i>
	YGL1011	YPS128	<i>MATa/α</i> , <i>ura3Δ0</i> ; <i>ura3Δ0</i> ; <i>leu2Δ0</i> ; <i>leu2Δ0</i> ; <i>lys2Δ0</i> ; <i>met15Δ0</i>
NA/NA	CC440	CC403 × CC407	<i>MATa/α</i> , <i>ura3::KanMX/ura3::KanMX</i> , <i>ho::HygMX/ho::HygMX</i> , <i>LYS2/lys2::URA3</i>
WA/NA	CC427	CC402 × CC407	<i>MATa/α</i> , <i>ura3::KanMX/ura3::KanMX</i> , <i>ho::HygMX/ho::HygMX</i> , <i>LYS2/lys2::URA3</i>
	CC435	CC403 × CC406	<i>MATa/α</i> , <i>ura3::KanMX/ura3::KanMX</i> , <i>ho::HygMX/ho::HygMX</i> , <i>LYS2/lys2::URA3</i>

Table S4: Glossary of strains with genetic constructs used in this study.

Gene	ID	Derived from	Genotype
CTF8	YGL1269	DBVPG6044	MATa, ho::HygMX, ura3::KanMX, ctf8::URA3
	YGL1270	YPS128	MATa, ho::HygMX, ura3::KanMX, ctf8::URA3
	YGL1271	DBVPG6044 × YPS128	MATa/α, ho::HygMX, ho::NatMX, ura3::KanMX, CTF8(NA)/ctf8(wa)::URA3
DEP1	YGL1272	DBVPG6044 × YPS128	MATa/α, ho::HygMX, ho::NatMX, ura3::KanMX, CTF8(WA)/ctf8(na)::URA3
	YGL1562	DBVPG6044	MATa, ho::HygMX, ura3::KanMX, dep1::URA3
	YGL1563	YPS128	MATa, ho::HygMX, ura3::KanMX, dep1::URA3
FPR1	YGL1570	DBVPG6044 × YPS128	MATa/α, ho::HygMX, ho::NatMX, ura3::KanMX, DEP1(NA)/dep1(wa)::URA3
	YGL1571	DBVPG6044 × YPS128	MATa/α, ho::HygMX, ho::NatMX, ura3::KanMX, DEP1(WA)/dep1(na)::URA3
	YGL2166	CC402	MATa, ura3::KanMX, ho::HygMX, fpr1::URA3
INP54	YGL2167	CC403	MATa, ura3::KanMX, ho::HygMX, fpr1::URA3
	YGL2181	FS174 × YGL2166	MATa/α, ura3::KANMX/ura3::KANMX, ho::HYGMX/ho::NATMX, fpr1::URA3/FPR1
	YGL2182	FS173 × YGL2167	MATa/α, ura3::KANMX/ura3::KANMX, ho::HYGMX/ho::NATMX, fpr1::URA3/FPR1
	YGL2184	FS173 × YGL2166	MATa/α, ura3::KANMX/ura3::KANMX, ho::HYGMX/ho::NATMX, fpr1(wa)::URA3/FPR1(NA)
	YGL2183	FS174 × YGL2167	MATa/α, ura3::KANMX/ura3::KANMX, ho::HYGMX/ho::NATMX, fpr1(na)::URA3/FPR1(WA)
	YGL2175	YGL2166	MATa, ura3::KanMX, ho::HygMX, fpr1::FPR1*
	YGL2193	YGL2167	MATa, ura3::KANMX, ho::HYGMX, fpr1::FPR1*
	YGL1564	DBVPG6044	MATa, ho::HygMX, ura3::KanMX, inp54::URA3
KOG1	YGL1565	YPS128	MATa, ho::HygMX, ura3::KanMX, inp54::URA3
	YGL1572	DBVPG6044 × YPS128	MATa/α, ho::HygMX, ho::NatMX, ura3::KanMX, INP54(NA)/inp54(wa)::URA3
	YGL1573	DBVPG6044 × YPS128	MATa/α, ho::HygMX, ho::NatMX, ura3::KanMX, INP54(WA)/inp54(na)::URA3
RNR2	YGL1264	DBVPG6044 × YPS128	MATa/α, ho::HygMX, ho::NatMX, ura3::KanMX, KOG1(NA)/kog1(wa)::URA3
	YGL1263	DBVPG6044 × YPS128	MATa/α, ho::HygMX, ho::NatMX, ura3::KanMX, KOG1(WA)/kog1(na)::URA3
	YGL2164	DBVPG6044	MATa/α, ura3Δ0, ura3Δ0, leu2Δ0, leu2Δ0, lys2Δ0, met15Δ0, RNR2/rnr2::URA3
RNR4	YGL2165	YPS128	MATa/α, ura3Δ0, ura3Δ0, leu2Δ0, leu2Δ0, lys2Δ0, met15Δ0, RNR2/rnr2::URA3
	YGL2391	CC427	MATa/α, ura3::KanMX/ura3::KanMX, ho::HygMX/ho::HygMX, LYS2/lys2::URA3, RNR2(NA)/rnr2(wa)::NATMX
	YGL2392	CC427	MATa/α, ura3::KanMX/ura3::KanMX, ho::HygMX/ho::HygMX, LYS2/lys2::URA3, RNR2(WA)/rnr2(na)::NATMX
	YGL2198	YGL1436	MATa/α, rnr2*::NATMX/RNR2
	YGL2189	YGL1436	MATa/α, rnr2*::NATMX
	YGL2174	CC402	MATa, ura3::KanMX, ho::HygMX, rnr4::URA3, aneuploidy in chr. VII (w/ RNR4)
	YGL2170	CC403	MATa, ura3::KanMX, ho::HygMX, rnr4::URA3
	YGL2177	FS174 × YGL2174	MATa/α, ura3::KANMX/ura3::KANMX, ho::HYGMX/ho::NATMX, rnr4::URA3/RNR4
TOR1	YGL2178	FS173 × YGL2170	MATa/α, ura3::KANMX/ura3::KANMX, ho::HYGMX/ho::NATMX, rnr4::URA3/RNR4
	YGL2180	FS173 × YGL2174	MATa/α, ura3::KANMX/ura3::KANMX, ho::HYGMX/ho::NATMX, rnr4::URA3/RNR4
	YGL2179	FS174 × YGL2170	MATa/α, ura3::KANMX/ura3::KANMX, ho::HYGMX/ho::NATMX, rnr4::URA3/RNR4
	YGL2194	YGL1001	MATa/α, ura3Δ0; ura3Δ0; leu2Δ0; leu2Δ0; lys2Δ0; met15Δ0; RNR4(WA)/rnr4(wa)::URA3
	YGL2196	YGL1011	MATa/α, ura3Δ0; ura3Δ0; leu2Δ0; leu2Δ0; lys2Δ0; met15Δ0; RNR4(NA)/rnr4(na)::URA3
	YGL2176	YGL2170	MATa, ura3::KanMX, ho::HygMX, rnr4::RNR4*
	YGL2168	CC402	MATa, ura3::KanMX, ho::HygMX, tor1::URA3
	YGL2169	CC403	MATa, ura3::KanMX, ho::HygMX, tor1::URA3
	YGL2185	FS174 × YGL2168	MATa/α, ura3::KANMX/ura3::KANMX, ho::HYGMX/ho::NATMX, tor1::URA3/TOR1
	YGL2186	FS173 × YGL2169	MATa/α, ura3::KANMX/ura3::KANMX, ho::HYGMX/ho::NATMX, tor1::URA3/TOR1
YNR066C	YGL2188	FS173 × YGL2168	MATa/α, ura3::KANMX/ura3::KANMX, ho::HYGMX/ho::NATMX, tor1(wa)::URA3/TOR1(NA)
	YGL2187	FS174 × YGL2169	MATa/α, ura3::KANMX/ura3::KANMX, ho::HYGMX/ho::NATMX, tor1(na)::URA3/TOR1(WA)
	YGL2201	YGL1431	MATa/α, tor1*::NATMX/TOR1
	YGL2191	YGL1431	MATa/α, tor1*/TOR1::NATMX
	YGL1566	DBVPG6044	MATa, ho::HygMX, ura3::KanMX, ynr066c::URA3
	YGL1567	YPS128	MATa, ho::HygMX, ura3::KanMX, ynr066c::URA3
	YGL1574	DBVPG6044 × YPS128	MATa/α, ho::HygMX, ho::NatMX, ura3::KanMX, YNR066C/ynr066c::URA3
	YGL1575	DBVPG6044 × YPS128	MATa/α, ho::HygMX, ho::NatMX, ura3::KanMX, YNR066C/ynr066c::URA3

Table S5: Sequence of primers used to amplify the genes containing putative driver mutations.

Gene	Orientation	Chr	Target		Sequence (TARGET)
			Start	End	
<i>DEP1</i>	fwd	I	128977	128996	CAGAGAGCTGGTCCAGTTCA
	rev	I	129573	129554	TGGCCTCATCTATCGCCTCT
<i>FPR1</i>	fwd	XIV	371600	371619	CCCTCCTGCCACAAGATTT
	rev	XIV	372170	372151	TGCCACCTTCCCAAAGACAG
<i>INP54</i>	fwd	XV	205005	205024	GCGAAAGTTGGCACTGCATA
	rev	XV	205624	205605	GCTACACAAGGGGATGAGCA
<i>RNR2</i>	fwd	X	392707	392726	CGTGCCGAAGCTTCTTTCTG
	rev	X	393245	393226	CATGCAAAGTCGGTGTGCAA
<i>RNR4</i>	fwd	VII	855968	855987	CAGGTTTTGCAATTGGGCA
	rev	VII	856843	856824	TACGACCACCCAACACCAAG
<i>TOR1</i>	fwd	X	565069	565088	AGCCAGATCCTACGGTGAGT
	rev	X	565652	565633	CCCAGGAACAGCCAATTCGA
<i>YNR066C</i>	fwd	XIV	753660	753679	TCGAATTCACTACCGTCGCC
	rev	XIV	754369	754348	GCCGCATATACACAATTAGCCT

Table S6: Primers used to engineer genetic constructs. Sequence of primers used to engineer gene deletions, as described in ‘Materials and methods’ (‘Engineered genetic constructs’) and illustrated in Fig. S8.

Gene	Marker	Orientation	Chr	Target		Sequence (TARGET, <i>ura3/natMX</i>)
				Start	End	
<i>CTF8</i>	<i>URA3</i>	fwd	VIII	486155	486230	TATATACACTTTACACAGAGCGTGAAGTCTGCGCCAAATAACATAAACAA ACAACCTCCGAACAATAACTAAGTACTcggcatcagagcagattgtactg
	<i>URA3</i>	rev	VIII	486709	486631	CTAACCTAATATAGCCAAAGGAGTGATAGAAAAAGAATTACTACTAT CATTGAGCCCAATAAACAGCTGAAAAGAAacaccgcagggttaataactg
<i>DEP1</i>	<i>URA3</i>	fwd	I	129210	129269	AACGGCAAAGTACAAGGGAAGGAAGCACAGAAGCAAGAGGAGGCGCATCG ATCGTGGCAGcggcatcagagcagattgtactg
	<i>URA3</i>	rev	I	130547	130488	ATAGCGTTACAACATATTTAAGAATAACAAAAAGAAGTGGTATGGGGTCC AGTGTGGCGGacaccgcagggttaataactg
<i>FPR1</i>	<i>URA3</i>	fwd	XIV	371821	371881	GATACTTACCATAAACATAAAATAAAAAGCAGAAAGCGCGCTCAATTGATA GTACTTTGCTTAcaccgcagggttaataactg
	<i>URA3</i>	rev	XIV	372287	372227	TAAAGTAAGGCCTTTCACCTAACTCGAGTATAAGCAAAAAATCAATCAA AACAAAGTAATAcggcatcagagcagattgtactg
<i>INP54</i>	<i>URA3</i>	fwd	XV	204671	204730	ACTGACGTTATCTGTTTCAGACATAAATGAAAACTTCTAGCTGCACAGC CCAGATCACTcggcatcagagcagattgtactg
	<i>URA3</i>	rev	XV	205945	205886	TAAGAGTAGGCTAACAAAGAAGAAAGTGAGACAAGAAAAATACAGCAGGA TTCTGACCGAAcaccgcagggttaataactg
<i>KOG1</i>	<i>URA3</i>	fwd	VIII	475924	475999	TAATAGATTATATATATATATATATATATATCTCTTTTTCAGCTAAATGA AAGAAAAAAGAAATGGCACATATcggcatcagagcagattgtactg
	<i>URA3</i>	rev	VIII	480750	480672	GAATGCATTTGGTTGTAGATTCTTTGATTACATTTAGCGAATCCTATT GCATGCAGAGAAGGGTAAAAGATACATAAacaccgcagggttaataactg
<i>RNR2</i>	<i>URA3</i>	fwd	X	392343	392403	CTCGATTGGCTATCTACCAAGAATCCAACCTTAATACCGTATTTATTT GTCCAATTACCcggcatcagagcagattgtactg
	<i>URA3</i>	rev	X	393664	393604	CGAAAGCCCACATAAAGAGATTGAAGAGACTCGTAAAAAGAAATATATA GAGAGATACTCacaccgcagggttaataactg
	<i>NatMX</i>	fwd	X	392343	392403	CTCGATTGGCTATCTACCAAGAATCCAACCTTAATACCGTATTTATTT GTCCAATTACCcgtacgctgcaggctcgac
	<i>NatMX</i>	rev	X	393604	393664	CGAAAGCCCACATAAAGAGATTGAAGAGACTCGTAAAAAGAAATATATA GAGAGATACTCacgatgaattcgagctcg
<i>RNR4</i>	<i>URA3</i>	fwd	VII	855203	855263	TATATATAAATATATATAAATAAAAGTGGCCAAGAATAAAAGAACGCACC CCGTGTTGACacaccgcagggttaataactg
	<i>URA3</i>	rev	VII	856362	856302	TACAAAAACAGATCTTTTGGCCACACAACCCCGCGCAACGCACACAAT TAGTTATTACcggcatcagagcagattgtactg
<i>TOR1</i>	<i>URA3</i>	fwd	X	559355	559415	TCACGAGAGAGTCTTTGGTAAAGTAAACATACATCAACCGGCTAGCAGG TTTGCAATTGATcggcatcagagcagattgtactg
	<i>URA3</i>	rev	X	566889	566829	AATGCGTAATACAAAAAATAAATAGTAAACAAGCAGGAAATGAAAAA TGACACCGCAGacaccgcagggttaataactg
	<i>NatMX</i>	fwd	X	559355	559415	TCACGAGAGAGTCTTTGGTAAAGTAAACATACATCAACCGGCTAGCAGG TTTGCAATTGATcgtacgctgcaggctcgac
	<i>NatMX</i>	rev	X	566829	566889	AATGCGTAATACAAAAAATAAATAGTAAACAAGCAGGAAATGAAAAA TGACACCGCAGatcgatgaattcgagctcg
<i>YNR066C</i>	<i>URA3</i>	fwd	XIV	753665	753724	TTCCTACCGTCCCAACGGAACCTGTCTTAACATAATTCGGCAGTAG GATTTGAGATcggcatcagagcagattgtactg
	<i>URA3</i>	rev	XIV	755095	755036	ATAAAGTTCCGAGCTTTGAAAAAAGCTTTGAACTAAGAAAAGGTAAGAG ATCCTCAATTacaccgcagggttaataactg

Table S7: Statistical support for variance components estimated using linear mixed models. Summary statistics for linear mixed models of the genetic cross, fitted using restricted maximum likelihood. Models were separately fitted for spores and hybrids in each environment. The number of unique backgrounds n_b is much greater than the number of degrees of freedom (d.o.f.) for the parameters being fitted. Each background b was measured in several technical replicates. We selected the best model by maximum AIC (labeled by §). The breakdown of variance components is shown in Fig. 4D and the models fits to the data are shown in Fig. S13.

Selection	Measurement	Type	Model	d.o.f.	Variance		Log-likelihood	AIC			
					r_F^2	r^2					
Hydroxyurea (YPD+HU)	Hydroxyurea (YNB+HU)	Spores $n_b = 92$	1	3	0.0000	0.9500	1813.367	-3627.063			
			2	4	0.1071	0.9504	1816.932	-3636.219			
			3 [§]	7	0.5338	0.9507	1841.92	-3697.223			
			4	8	0.5338	0.9509	1839.372	-3695.832			
			Hybrids $n_b = 2013$	1	3	0.0000	0.8045	6535.699	-13 075.484		
				2	5	0.0652	0.8044	6608.318	-13 230.265		
		Hydroxyurea (YPD+HU)	Control (YNB)	Spores $n_b = 92$	1	3	0.0000	0.8914	1918.357	-3837.994	
					2	4	0.0381	0.8924	1917.974	-3840.051	
					3	7	0.0605	0.8954	1911.224	-3836.707	
					4 [§]	8	0.1559	0.8957	1913.807	-3846.480	
					Hybrids $n_b = 2013$	1	3	0.0000	0.8335	9435.532	-18 875.965
						2	5	0.0009	0.8337	9429.119	-18 874.079
Rapamycin (YPD+RM)	Rapamycin (YNB+RM)			Spores $n_b = 104$	1	3	0.0000	0.9815	438.8476	-875.752	
					2	4	0.0924	0.9817	443.2374	-884.134	
					3	7	0.8146	0.9815	524.504	-1054.421	
					4 [§]	8	0.8699	0.9815	542.2816	-1094.737	
					Hybrids $n_b = 2271$	1	3	0.0000	0.9583	2368.301	-4738.294
						2	5	0.0355	0.9584	2407.246	-4819.913
		Rapamycin (YPD+RM)	Control (YNB)	Spores $n_b = 104$	1	3	0.0000	0.9217	1038.794	-2078.815	
					2	4	0.0011	0.9224	1036.569	-2076.940	
					3	7	0.1711	0.9239	1039.674	-2092.692	
					4 [§]	8	0.3953	0.9235	1054.494	-2128.413	
					Hybrids $n_b = 2270$	1	3	0.0000	0.9065	11394.15	-22 793.196
						2	5	0.0173	0.9066	11408.58	-22 832.161
					3	17	0.0593	0.9072	11418.03	-22 915.694	
					4 [§]	18	0.0697	0.9071	11428.48	-22 941.867	